Stratiform Precipitation Processes in Cyclones Passing over a Coastal Mountain Range

JOSEPH P. ZAGRODNIK AND LYNN A. MCMURDIE

University of Washington, Seattle, Washington

ROBERT A. HOUZE JR.

University of Washington, Seattle, and Pacific Northwest National Laboratory, Richland, Washington

(Manuscript received 2 June 2017, in final form 9 January 2018)

ABSTRACT

The Olympic Mountains Experiment (OLYMPEX) documented precipitation and drop size distributions (DSDs) in landfalling midlatitude cyclones with gauges and disdrometers located at various distances from the coast and at different elevations on the windward side of the mountain range. Statistics of the drop size and gauge data for the season and case study analysis of a high-rainfall-producing storm of the atmospheric river type show that DSDs during stratiform raining periods exhibit considerable variability in regions of complex terrain. Seasonal statistics show that different relative proportions of drop sizes are present, depending on synoptic and mesoscale conditions, which vary within a single storm. The most frequent DSD regime contains modest concentrations of both small and large drops with synoptic factors near their climatological norms and moderate precipitation enhancement on the lower windward slopes. The heaviest rains are the most strongly enhanced on the lower slope and have DSDs marked by large concentrations of small to medium drops and varying concentrations of large drops. During the heavy-rain period of the case examined here, the low-level flow was onshore and entirely up terrain, the melting level was ~2.5 km, and stability moist neutral so that large amounts of small raindrops were produced. At the same time, melting ice particles produced at upper levels contributed varying amounts of large drops to the DSD, depending on the subsynoptic variability of the storm structure. When the low-level flow is directed downslope and offshore, small-drop production at low altitudes is reduced or eliminated.

1. Introduction

The west coast of North America is frequented by landfalling extratropical cyclones from the Pacific Ocean during the fall through early spring. When these storms pass over coastal mountain ranges, they produce copious precipitation on the windward slopes, frequently contributing to hazards such as flooding and landslides. These storms are also responsible for the accumulation of snow at higher elevations, which is crucial for summer water supply. Understanding the processes responsible for producing precipitation in these storms has been the subject of numerous past field programs (e.g., Hobbs et al. 1971; Houze et al. 1976; Hobbs 1978; Matejka et al. 1980; Bond et al. 1997; Ralph et al. 1999; Stoelinga et al. 2003; Houze and Medina 2005; Medina et al. 2007). Similar processes also occur on the west coast of South America (Barrett et al. 2009; Viale et al. 2013; Garreaud et al. 2016; Massmann et al. 2017).

Nagle and Serebreny (1962) synthesized the detailed structure of the precipitation pattern in maritime frontal cyclones approaching the West Coast of the United States, and several studies have refined this model (Houze et al. 1976; Matejka et al. 1980; Medina et al. 2007). The idealized structure in Fig. 1 divides storms into four sectors: prefrontal (early), frontal (middle), postfrontal (late), and warm sector. The prefrontal sector contains the leading edge of precipitation ahead of the occluded or warm front and is associated with warm advection and rising melting levels. The frontal sector is a broad, elongated cloud shield within which a cold or

---

Denotes content that is immediately available upon publication as open access.

Corresponding author: Joseph P. Zagrodnik, jzagrod@uw.edu

DOI: 10.1175/JAS-D-17-0168.1

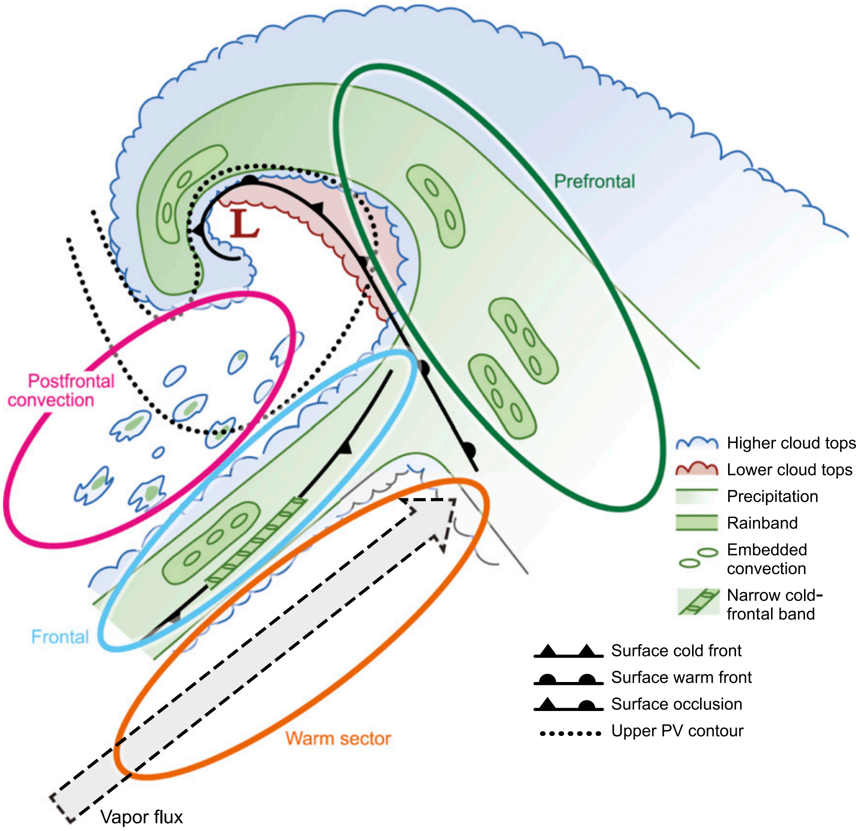

FIG. 1. Idealized diagram of the sectors of an extratropical cyclone passing over the Olympic Mountains. Reproduced from Houze et al. (2017).

occluded front's circulation generates banded precipitation. Sometimes the cold front is sharp, but more often over the ocean the temperature change in the cold-frontal zone is weak. Within these storm sectors are embedded rainbands and other mesoscale and convective elements of enhanced precipitation. The broad, moist warm sector located ahead of the cold-frontal zone and to the south of the warm-frontal region sometimes contains an extensive narrow zone of water vapor flux commonly called an ''atmospheric river'' (Newell et al. 1992; Zhu and Newell 1994, 1998; Ralph et al. 2004; Warner et al. 2012). Behind the cold front, the postfrontal sector consists mainly of small-scale convective showers, which sometimes form into bands or other mesoscale features. This study focuses on the sectors with predominantly stratiform precipitation. Postfrontal convection is left to future work.

It is well known that the precipitation associated with these landfalling extratropical storms is enhanced on the windward slopes of west-coastal mountains. Neiman et al. (2002) used wind profiler observations to show that the rain rate on windward slopes in the California coastal range is highly correlated with the intensity of unblocked low-level flow. When the low-level flow is blocked, rain rate correlates with the flow intensity near the mountaintop, likely from the low-level flow lifting over the blocking. Minder et al. (2008) used case studies and climatologies from both rain gauges and high-resolution model output to demonstrate that enhanced precipitation growth by collection of cloud water occurs during periods when stable flow ascends over the windward slopes of the Olympic Mountains. White et al. (2003) and Kingsmill et al. (2006) used profiling radars to show that collision–coalescence can produce precipitation on the low-elevation windward slopes of the California coastal range without radar indication of ice-phase hydrometeors. Martner et al. (2008) further illustrated that this ''nonbrightband rain'' was associated with larger concentrations of small drops, while the presence of melting ice hydrometeors from deeper clouds, when present, shifted the drop size distribution (DSD) toward larger drop sizes and smaller drop concentrations. These studies have highlighted how precipitation production depends on the relative role of warm processes (condensation/collision–coalescence) and cold processes (riming, accretion, and aggregation). Much work remains, however, to understand the factors that determine the relative roles of the warm and cold processes, as they typically occur within the same storm.

This paper aims to shed light on how the relative importance of warm and cold processes varies within storms passing over west-coastal mountains.

The 2015/16 Olympic Mountains Experiment (OLYMPEX; Houze et al. 2017) provides unprecedented data for this purpose. OLYMPEX was a physical and hydrologic ground validation project for the U.S.–Japan Global Precipitation Measurement (GPM) satellite mission. However, it was conducted in a way that also facilitates study of the mechanisms of precipitation in Pacific frontal systems and how passage of these storms over coastal mountains modifies the precipitation processes. OLYMPEX deployed extensive observational assets, including four NASA research aircraft, four dual-polarization Doppler research radars, rain gauges, particle size distribution measurements, and Micro Rain Radars at a variety of elevations ranging from the coast to mid-elevations. At the latitude of OLYMPEX, the melting layer in storms arriving from the Pacific Ocean typically is at a relatively low altitude so that both low-level warm growth of drops and melting ice particles from higher levels contribute to the precipitation but to differing degrees depending on the sector of the storm passing over the region and on smaller-scale variability within each storm sector. This study focuses on ground-based measurements of DSDs in OLYMPEX in combination with synoptic and radar data. The goal is to elucidate the mechanisms of precipitation growth and how these processes are enhanced over the Olympic Mountains. We analyze the statistics of DSD data over the season in which OLYMPEX occurred, and to further elucidate the precipitation processes, we examine an atmospheric river–type storm that produced the heaviest precipitation during OLYMPEX.

2. Data

a. Synoptic data

The synoptic data used in this study to describe the dynamic and thermodynamic properties of the maritime flow impinging upon the mountains are from the North American Regional Reanalysis (NARR; Mesinger et al. 2006). The NARR dataset (NOAA/OAR/ESRL PSD 2004) has 3-h time resolution, 32-km horizontal grid spacing, and 25-hPa vertical resolution. The 925-hPa wind magnitude and direction provides low-level flow context. NARR includes a derived 3-h horizontal water vapor flux accumulation parameter that we converted to instantaneous integrated vapor transport (IVT; $\mathrm{kg\,m^{-1}\,s^{-1}}$) to compare to the analyses in atmospheric river studies such as Neiman et al. (2008). The melting level is the height of the highest NARR pressure level with a temperature above 0°C. Similar to Medina and Houze (2015), the upstream low-level stability is evaluated using the dry and moist Brunt–Väisälä frequency, N_d^2 and N_m^2, respectively, calculated for the 950–850-hPa layer according to Durran and Klemp (1982). These parameters are evaluated at the 0.3° grid box centered on the coast upstream of the Olympic Mountains at the location of the NASA dual-polarization S-band Doppler radar (NPOL; marked in Fig. 2) installed during OLYMPEX.

b. OLYMPEX data

Surface sites installed for OLYMPEX collected precipitation and drop size distribution data during the entire cold season from 10 October 2015 to 30 April 2016 (Petersen et al. 2017). Particle Size and Velocity 2 (PARSIVEL) disdrometers were collocated with either pairs of tipping-bucket rain gauges at low-elevation sites or Pluvio^2-400 weighing buckets designed to measure either liquid or frozen precipitation at high-elevation sites. Figure 2 indicates the five ground sites used in this study and the total precipitation observed at these sites during the entire cold season. Table 1 lists exact locations and elevations. The three low-elevation sites—Fishery, Bishop Field, and Graves Creek—were within the Quinault Valley. Prairie Creek was located at an intermediate elevation, often below the snow line, on the first significant ridge encountered by westerly or southwesterly flow. This ridge was previously instrumented by Minder et al. (2008). The Wynoochee site was in an area of higher terrain to the south of the Quinault Valley on the south side of the Olympic Mountains. The rain gauges and Pluvio did not have wind shields, so there was likely some undercatch (Nešpor and Sevruk 1999). A collocated NOAA Climate Reference Network (CRN) site with a wind-shielded gauge at Bishop Field differed from the OLYMPEX gauges by only 3%–5%. The windier Wynoochee site compared favorably with a better-protected tipping-bucket site on the same ridge in raining periods. Undercatch was likely greater in snowing periods, but the NARR melting level was only below 1.2 km in 19 of the 181 three-hour periods, and comparison of precipitation measurements between the wind-shielded Buckinghorse Snowpack Telemetry (SNOTEL) and Wynoochee sites (not shown) suggests that the conclusions drawn from the Wynoochee site are applicable elsewhere in the Olympic Mountains.

The case study discussed in section 4 used data from two radars. The NPOL was located on a coastal hill with direct views of the Quinault Valley. The NSF-sponsored mobile dual-polarization X-band Doppler radar [Doppler on Wheels (DOW)] of the Center for Severe Weather Research was operated in the Quinault Valley where it scanned underneath the lowest NPOL beam in order to resolve finer details of the processes within the valley. We focus here on a vertical cross section (RHI)

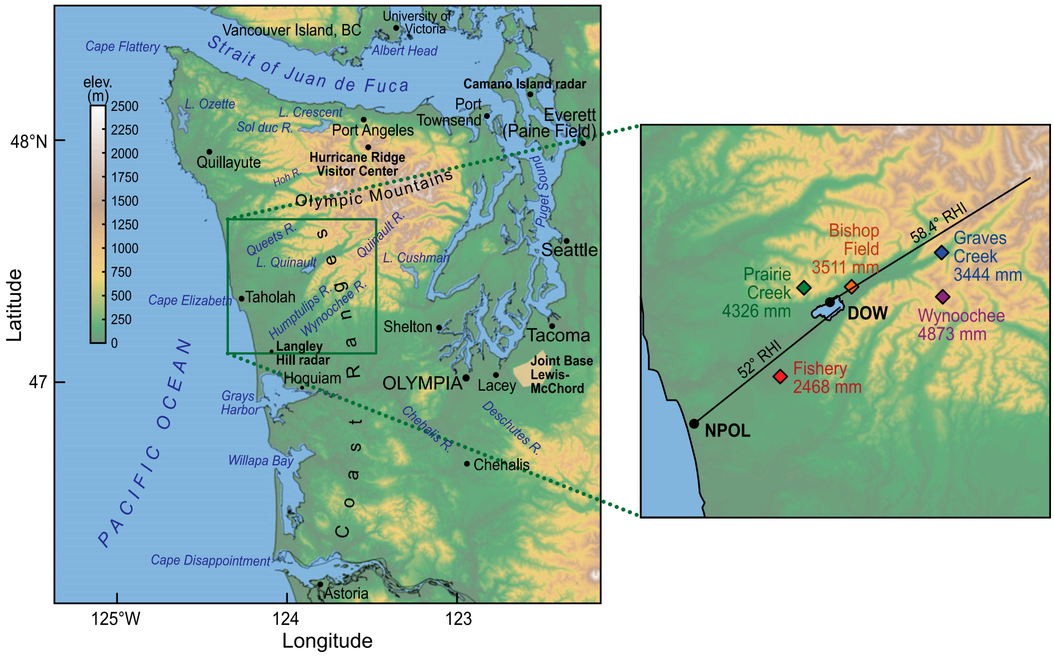

FIG. 2. (left) Locations of OLYMPEX radars and ground sites used in this study. (right) The black line denotes the 52° NPOL RHI and the 58.4° DOW RHI, including the total measured precipitation from 10 Oct 2015 to 30 Apr 2016.

along the DOW 58.4° azimuth and NPOL 52° azimuth. This configuration diagrammed by the solid line in Fig. 2 accounts for the rightward bend of the Quinault Valley.

c. *Selection of 3-h samples*

To compile statistics, we combined all of the rain gauge and disdrometer data into 3-h periods centered on the synoptic times of the NARR data (0000, 0300 UTC, etc.). Other recent statistical studies of disdrometer data (e.g., Thompson et al. 2015) have used a much shorter (usually 1 min) interval because they were analyzing convective precipitation, which occurs on short time and space scales. In OLYMPEX, the precipitation was primarily stratiform, and the DSDs remained consistent for many hours at a time, tending to shift only when there were substantial synoptic or mesoscale environmental changes. To be selected for inclusion in our statistics, a 3-h period must have had three consecutive hours with precipitation rates $>1\,\mathrm{mm\,h^{-1}}$ at one or more ground sites. To focus on stratiform precipitation periods, we did not include postfrontal convective periods. Most postfrontal periods did not meet the $1\,\mathrm{mm\,h^{-1}}$ criterion, and those that did were excluded based on subjective examination of radar data for the presence of discrete convective cells. However, some postfrontal periods with predominantly nonconvective character such as comma clouds, occluded fronts, or cutoff lows did meet the continuous 3-h consecutive precipitation criteria and were retained in the dataset. Some of the accepted stratiform periods had shallow embedded (generating) cells aloft. No deep convection was observed in any of the time periods that met the 3-h consecutive rainfall criteria. Some precipitation data were eliminated from individual sites because of snow contamination in the tipping buckets, isolated power outages, and overflowing of the Wynoochee Pluvio bucket. Mean differences between various samples of 3-h rain rates or synoptic parameters are compared with two-sided *t* tests and considered significant at the 95% confidence level or greater.

TABLE 1. Description of the five OLYMPEX ground sites used in this study.

Site	Elevation (m)	Latitude	Longitude	Description	Instrument(s) used
Fishery	52	47.36°	−123.99°	Windward, upstream, low elevation	PARSIVEL, MRR, tipping buckets
Bishop Field (CRN)	85	47.54°	−123.68°	Windward, front of valley, low elevation	PARSIVEL, tipping buckets
Prairie Creek	543	47.51°	−123.93°	Windward, front of valley, midelevation	PARSIVEL, tipping buckets
Graves Creek	180	47.57°	−123.58°	Windward, interior valley, low elevation	PARSIVEL, tipping buckets
Wynoochee	1020	47.5°	−123.58°	Windward, interior, high elevation	Pluvio

d. Analysis of disdrometer data

The PARSIVEL measurements were used for the DSD data since they were installed for the full 2015/16 cold season. The PARSIVEL is a laser optical disdrometer that measures the size and fall velocity of hydrometeors passing through a 180 mm × 30 mm × 1 mm sheet laser. The raw output contains 32 size and velocity bins from 0.2 to 25 mm diameter and 0.2 to 20 $\mathrm{m\,s^{-1}}$ velocity, respectively, with 10-s time resolution. The PARSIVEL output assumes drops are falling straight down and corrects drops greater than 1 mm for oblateness. The 3-h DSDs were computed following Eq. (6) of Tokay et al. (2014) using terminal fall velocities from Atlas et al. (1973) and a time interval of 3 h centered on the synoptic times (e.g., 0000, 0300 UTC, etc.). Within each 3-h period, 10-s periods with error flags in the PARSIVEL data or frozen precipitation were removed. If less than 50% of the 3-h period had good data, the entire 3-h period was removed. The final accepted PARSIVEL dataset included 209 three-hour periods at the Fishery, 217 at Prairie Creek, 217 at Bishop Field, and 192 at Graves Creek. Over 90% of the raw PARSIVEL and gauge data that met the 1 $\mathrm{mm\,h^{-1}}$ criterion was accepted. The 3-h DSDs were the basis for the analysis of the season-long statistics discussed in section 3. The DSDs were calculated in 1-h segments for analysis of the case study presented in section 4. For high resolution of DSDs of the case study, the DSDs were calculated in 5-min segments.

To make comparisons between DSDs from different time periods, it is important to use an appropriate DSD model. DSDs typically can be approximated by a gamma distribution:

$$N(D) = N_o D^{\mu} \exp(-\Lambda D), \tag{1}$$

where D is drop diameter and the parameters of the distribution are the slope parameter Λ, intercept parameter N_o, and shape parameter μ. Here, slope and intercept refer to a plot of $\log N_o$ on the y axis versus D on the x axis. A series of papers (Ulbrich 1983; Willis 1984; Testud et al. 2001; Bringi et al. 2002, 2009; Thompson et al. 2015) have led to the understanding that Λ and μ are interrelated and, consequently, that a gamma distribution of a given liquid water content LWC can be represented by an exponential distribution for which the intercept parameter N_w ($\mathrm{m^{-3}\,mm^{-1}}$) is given by

$$N_w = \frac{1.81 \times 10^5\,\mathrm{LWC}}{\pi \rho_w D_o^4}, \tag{2}$$

where the density of liquid water has the value 1 $\mathrm{g\,cm^{-3}}$, LWC has units of $\mathrm{g\,m^{-3}}$, and D_o is in mm. The N_w is referred to as the "normalized intercept parameter." Because every combination of N_w and D_o correspond to a given LWC, if the DSD is approximately a gamma distribution, an N_w–D_o coordinate system is useful for characterizing observed DSDs because each measured DSD can be mapped using its specific combination of N_w and D_o. Figures 3, 4, and 5 use this coordinate system, wherein N_w is a proxy for the number concentration of drops and D_o is a proxy for their predominant drop size. For each observed combination of N_w and D_o, we can indicate the number of observations, mean rain rate, and synoptic parameters observed at the time of the DSD measurement. As a result of using this plotting method, our figures are directly comparable to those of Thompson et al. (2015), who studied DSDs in tropical oceanic convective storms, in contrast with the orographically influenced stratiform midlatitude frontal systems examined here.

3. Relationship between DSD, synoptic environment, and orographic enhancement for the full 2015/16 cold season

This section describes statistics of the stratiform precipitation observations for the full 2015/16 cold season. As discussed in section 2d, Fig. 3 shows the rain rate R for each of the combinations of 3-hourly values of D_o and N_w measured by the OLYMPEX disdrometers over the whole season of the campaign. Results are shown for two windward sites:

- Fishery—Representing near-coastal conditions
- Prairie Creek—Representing conditions at medium elevation on the windward side of the mountains, where some of the greatest amounts of rain were observed

The average rain rates corresponding to different combinations of (N_w, D_o) in Figs. 3c,d were calculated from the dual tipping buckets rather than the PARSIVEL estimates, which depend on particle fall velocity assumptions.[1] The rain rate of the most frequent DSD was 2.7 $\mathrm{mm\,h^{-1}}$ at both sites. This rate is similar to the mean rain rate during the entire season at Fishery of 2.5 $\mathrm{mm\,h^{-1}}$ but considerably less than the 4.7 $\mathrm{mm\,h^{-1}}$ mean rain rate at higher-elevation Prairie Creek.

The distributions shown in Fig. 3 for Prairie Creek and Fishery have the same general shape and similar modes to each other, with the frequency maxima in the midranges of number and size (highlighted by the white dashed box in Fig. 3). The shape of these distributions,

---

[1] The corresponding rain-rate bins for a given N_w and D_o between Figs. 3c and 3d may differ slightly because 1) the bins contain different samples of N_w and D_o and 2) the PARSIVEL and tipping-bucket gauges estimate slightly different rain rates.

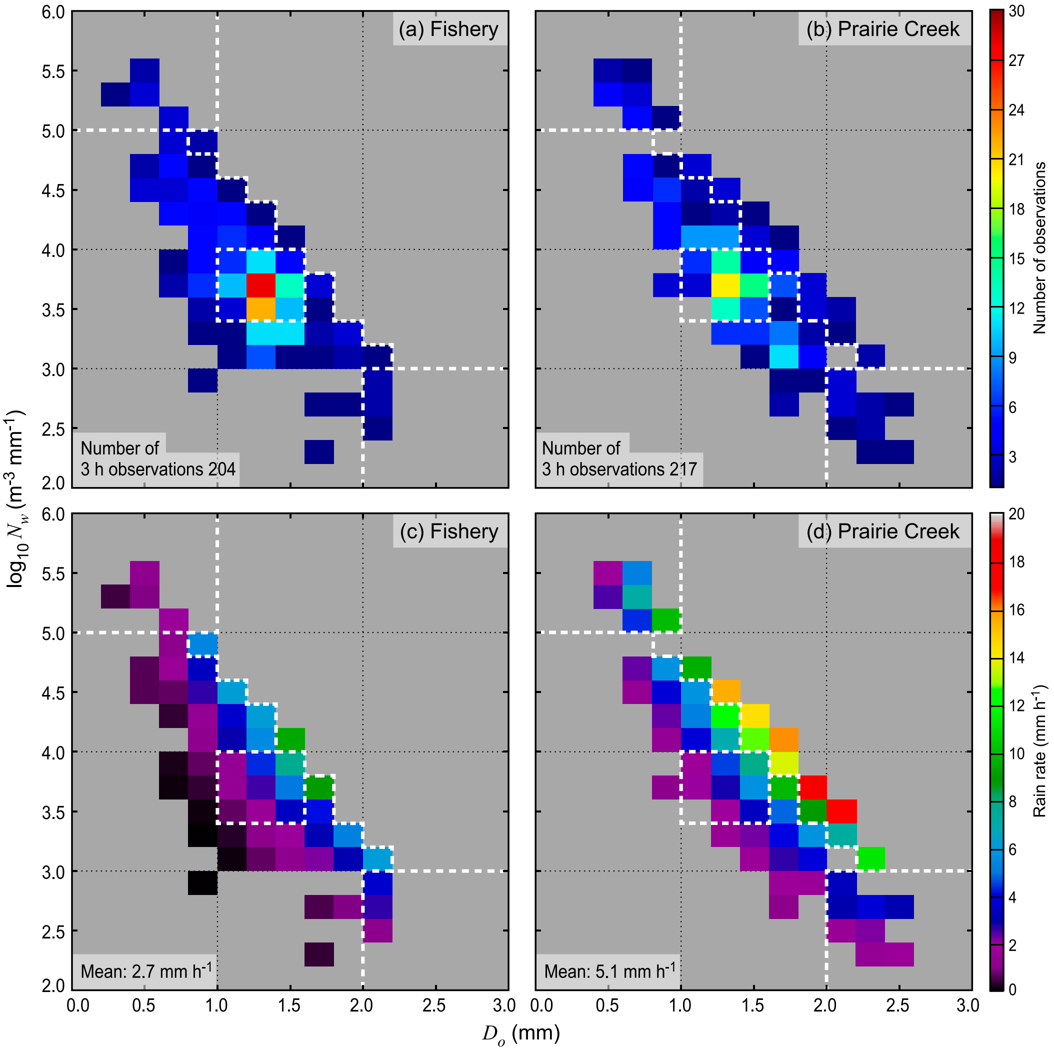

FIG. 3. Two-dimensional histograms of 3-h DSDs binned by $\log_{10}(N_w)$ and D_o at (left) Fishery and (right) Prairie Creek. (a),(b) Number of observations in each bin. (c),(d) Average rain rate measured by dual tipping buckets. The dashed white lines denote the four DSD regimes: the upper-left box corresponds to large quantities of small drops, the middle box corresponds to the most frequent regime, the lower-right box corresponds to small numbers of large drops, and the region to the right of the diagonal stair-step line corresponds to the heavy-rain regime.

which are for midlatitude cyclonic stratiform precipitation, are similar to those seen in studies of convective precipitation (e.g., Thompson et al. 2015), indicating that raindrop size distributions have a fundamental similarity regardless of dynamical context. A notable difference from the convective studies is that the stratiform precipitation analyzed here over 3-h samples has fewer outliers than in the 1-min interval statistics of convective rain (Thompson et al. 2015).

Much of the contrast between Fishery and Prairie Creek is in the outliers of the distributions. The Prairie Creek distribution is shifted such that there are more bins to the right of the stair-step diagonal line for Prairie Creek in Fig. 3. Especially notable is that rain rates >10 mm h^{-1} were much more common at Prairie Creek than at Fishery. These periods of greater rainfall, especially those exceeding 15 mm h^{-1}, were associated with landslides, road washouts, and rapid increases in the level of Lake Quinault.[2] The DSDs for rain rates >10 mm h^{-1} at Prairie Creek were highly variable, sometimes favoring higher N_w, larger D_o, or both, relative to the most frequent DSD.

The remainder of this section examines the N_w–D_o distribution at Prairie Creek, the rainier site located at midelevation on the windward slope of the Olympic

---

[2] Lake Quinault is a natural lake on the lower Quinault River.

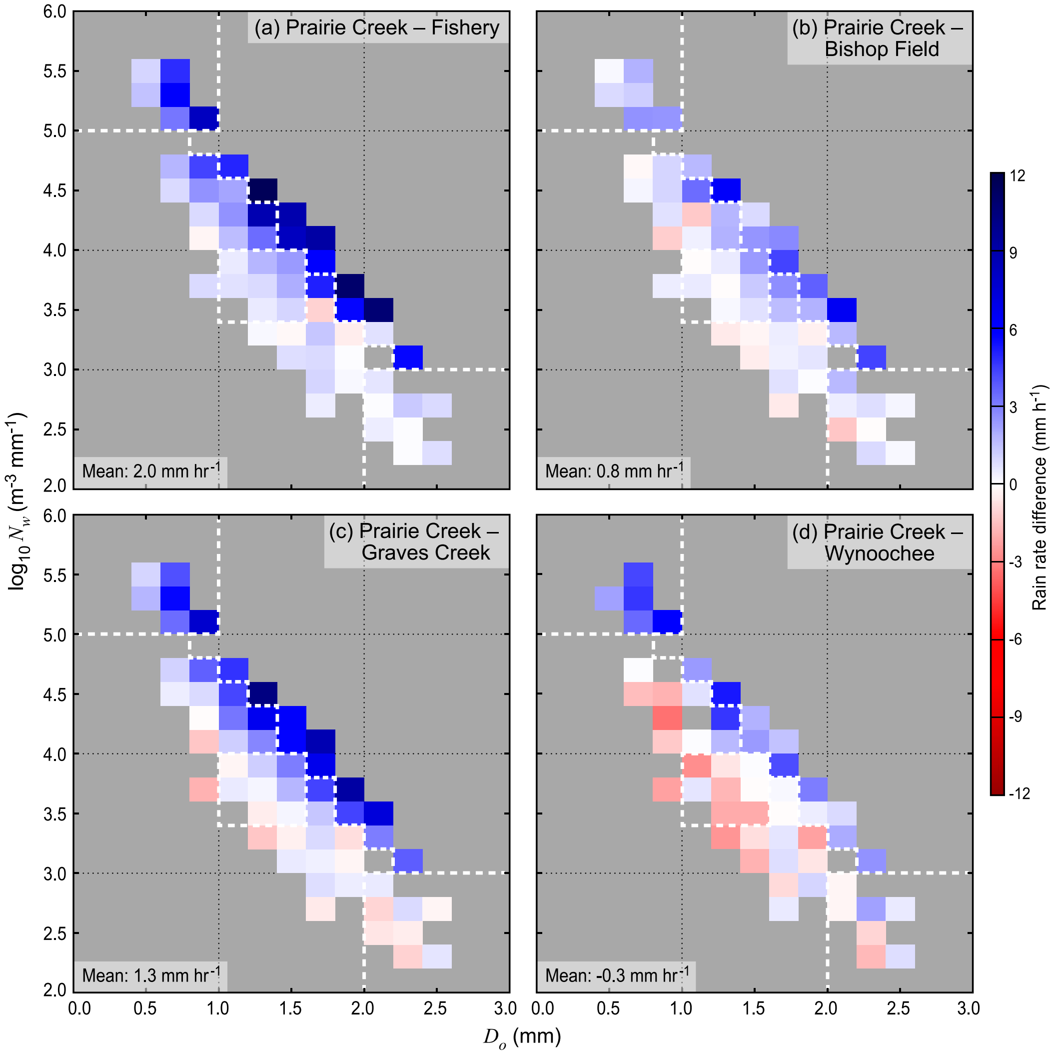

FIG. 4. Difference in precipitation rate measured by precipitation gauges (dual tipping buckets or Pluvio weighted bucket) between Prairie Creek and the four other ground sites. The data are binned by the Prairie Creek 3-h DSD as in Fig. 3b. The white dashed lines are as in Fig. 3.

Mountains. Figure 4 shows Prairie Creek DSDs with the bins color coded by the difference in average precipitation rate between Prairie Creek and four ground sites with blue shaded areas denoting DSDs where Prairie Creek had more precipitation than the comparison site and red boxes where Prairie Creek had less. Figure 5 shows the Prairie Creek DSDs with the bins color coded by synoptic environment parameters derived from the NARR data: average melting level (Fig. 5a); integrated water vapor transport (IVT; Fig. 5b); 925-hPa wind speed (Fig. 5c); 925-hPa wind direction (Fig. 5d); dry Brunt–Väisälä frequency, N_d^2 (Fig. 5e); and moist Brunt–Väisälä frequency, N_m^2 (Fig. 5f). Other variables were tested, but consistent with Neiman et al. (2002), we found that temperature, low-level flow, and static stability were the factors most strongly related to precipitation processes affected by topography. In the following subsections, we organize the discussion of these figures around four regimes in N_w–D_o space: most frequent DSDs, small-drop-dominated DSDs, large-drop-dominated DSDs, and DSDs in the heaviest-rain events.

a. The most frequently occurring distributions (moderate N_w and D_o)

The most frequent drop size regime (box outlined by white dashes in the middle of Figs. 3, 4, and 5) is where D_o ranges from 1.0 to 1.6 mm and N_w ranges from 3.4 to 4.0 $\mathrm{m^{-3}\,mm^{-1}}$. Figure 5 shows that 1) the average melting level of this regime was 1870 m, slightly below the average melting level of 1920 m observed for the full

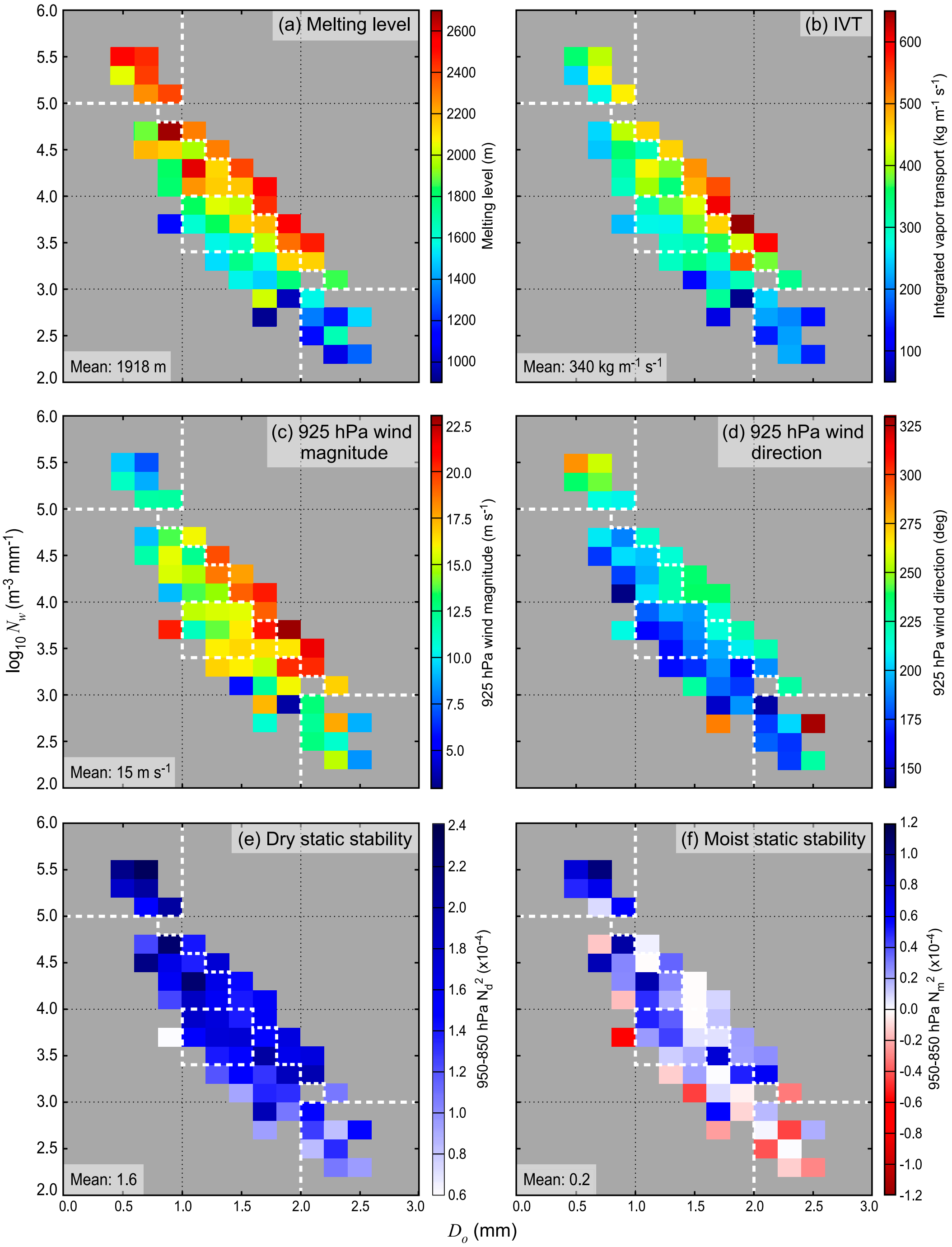

FIG. 5. Average synoptic environmental parameters calculated at the NARR grid point closest to NPOL. (a) Melting level (m), (b) IVT (kg m^{-1} s^{-1}), (c) 925-hPa wind speed (m s^{-1}), (d) 925-hPa wind direction (°), (e) dry Brunt–Väisälä frequency (N_d^2), and (f) moist Brunt–Väisälä frequency (N_m^2). The data are binned by the Prairie Creek 3-h DSD as in Fig. 3b. The white dashed lines are as in Fig. 3.

sample; 2) the IVT was 250–300 kg m^{-1} s^{-1}; 3) the 925-hPa wind speed averaged 15 m s^{-1}, generally from the south; and 4) both N_d^2 and N_m^2 were greater than zero, indicating statically stable conditions upstream. Despite modest IVT, none of the other environmental parameters are especially favorable for low-level enhancement on the southwest side of the Olympic Mountains, consistent with the modest enhancement between Fishery and Prairie Creek, which lie in the southwest-facing Quinault Valley.

Figure 4 shows that Fishery and Graves Creek had rain rates lower than Prairie Creek in this regime. In contrast, the rain rates at the highest-elevation Wynoochee site were greater than at Prairie Creek by 1.2 mm h^{-1}. All of these differences passed statistical significance testing. Wynoochee received more precipitation than any other OLYMPEX site (Fig. 2) but was often not the highest during individual events, including the case examined in section 4 of this paper.

b. *Distributions with large quantities of small drops (high N_w and small D_o)*

We define the regime of "large quantities of small drops" as $\log_{10}N_w$ greater than 5 m^{-3} mm^{-1} and D_o less than 1 mm. Compared to the most frequent distribution; the small-drop regime has a 410-m-higher melting level and 9.7 m s^{-1} weaker low-level flow from the west-southwest (Fig. 5). These differences are statistically significant at levels of 95% or greater. The IVT is slightly higher than the most frequent regime, but the difference is not statistically significant. The upstream flow in this small-drop regime is statically stable on average.

The overall DSD in this regime (Fig. 6) favors small drops, as seen in the nonconvective, nonbrightband rain of White et al. (2003), Martner et al. (2008), and Massmann et al. (2017). Following the brightband/nonbrightband algorithm from Massmann et al. (2017), a vertically pointing Micro Rain Radar (MRR) at the Fishery site indicated nonbrightband rain by their criteria in 9% of the 30-min segments within the 3-h raining periods used in this study. This nonbrightband precipitation was most frequent within the small-drop regime. However, a bright band was present in 74% of 30-min periods classified as large numbers of small drops (Table 2). While a large dataset of MRR data is not available at other OLYMPEX sites, a limited sample from 1 November 2015 through 15 January 2016 at Bishop Field observed nonbrightband rain in only 21 of 366 (6%) 30-min periods covering all DSD regimes. In a broader study encompassing four rainy seasons, White et al. (2015) also reported relatively low frequencies (14.4%) of nonbrightband rain near the Washington coast. Therefore, while nonbrightband rain may be more important in other coastal mountainous regions, it cannot be used to explain the DSD variability during stratiform steady raining periods in OLYMPEX.

Figure 4 shows that the average precipitation rate in the small-drop regime at Prairie Creek is modestly but not significantly higher than Fishery and Bishop Field (Fig. 4a) and significantly higher than Graves Creek and Wynoochee (Figs. 4b,c,d) at a 99% confidence level. The absence of large drops and the weak low-level flow suggest that this orographic enhancement pattern has weak synoptic forcing and is predominantly the consequence of condensation and rapid fallout of small drops near the front of the Olympic Mountain barrier where the flow is initially lifted.

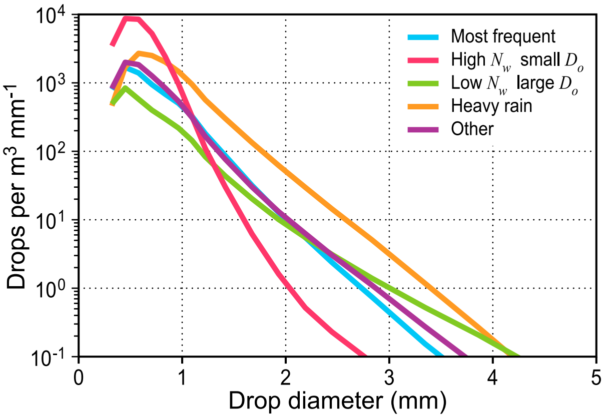

FIG. 6. Overall DSDs at Prairie Creek for each of the four DSD regimes described in section 3 of the text and the unclassified "other" category.

c. *Distributions with small quantities of large drops (low N_w, large D_o)*

The regime with smaller quantities of large drops is defined by $N_w < 3$ m^{-3} mm^{-1} and $D_o > 2$ mm. Figure 6 shows that relative to the most frequent regime, the large-drop regime has fewer drops smaller than 2 mm and more drops larger than 2.5 mm. The plots in Fig. 5 clearly show that this regime was characterized by cold conditions, with a mean melting level of 1400 m; weak IVT averaging 200 kg m s^{-1}; light to moderate low-level winds, generally from the south but occasionally from the west or northwest;[3] and frequent conditional instability (54% of 3-h periods), typically a consequence of cold air aloft. The differences between the synoptic conditions of melting-level height, IVT, and stability in this regime are statistically significant from those in the most frequent regime, whereas the 925-hPa wind speed and direction are not. In this low-N_w–large-D_o regime, orographic enhancement is negligible on average with no statistically significant differences in precipitation rate between the five OLYMPEX sites (Fig. 4). The lack of moisture and the weak low-level flow evidently limited the ability of this regime to produce strong orographic enhancement, while cold processes above the

---

[3] From synoptic experience, prefrontal sectors traversing the OLYMPEX region with low melting levels generally tend to be accompanied by southerly or southeasterly flow, while in occluded fronts or colder cyclones tracking from the northwest, the flow tends to be westerly or northwesterly.

TABLE 2. Frequency of occurrence and contribution to the total rainfall of the four DSD regimes at four ground sites. The "other" category encompasses 3-h DSDs that fall outside of the four DSD regimes. The percentage of brightband rain is also included for 752 thirty-minute MRR observation periods at the Fishery site following the methodology of Massmann et al. (2017).

	Fishery (204 obs)			Bishop Field (217 obs)		Prairie Creek (217 obs)		Graves Creek (192 obs)	
Category	Percentage of 3-h periods	Percentage of total rainfall	Percentage of bright band	Percentage of 3-h periods	Percentage of total rainfall	Percentage of 3-h periods	Percentage of total rainfall	Percentage of 3-h periods	Percentage of total rainfall
Most frequent	48	58	90	36	29	34	27	50	52
High N_w, small D_o	3	2	74	6	5	6	5	0	0
Low N_w, large D_o	2	3	92	6	3	6	3	2	2
Heavy rain	1	1	95	13	31	14	34	0	0
Other	46	36	93	39	32	40	31	47	46

bright band nevertheless generated medium- to large-sized raindrops.

d. Distributions during heavy rain (high N_w and large D_o)

The highest rain rates observed at the OLYMPEX sites concentrate to the upper right of the diagonal stair-step boundary in Figs. 3, 4, and 5. We therefore call this part of the N_w–D_o diagram the *heavy-rain regime*. The characteristics of the heavy-rain regime include elevated values of N_w, D_o, or both; an average rain rate of 13.3 mm h^{-1}; and considerable orographic enhancement at low to midelevations near the front of the barrier, when the Bishop Field and Prairie Creek sites often had 8–12 mm h^{-1} greater rain rates than near-coastal sites such as Fishery. The overall DSD in this regime has the same shape as the most frequent regime (Fig. 6) but with much greater concentrations of drops of all sizes above 0.5-mm diameter.

This regime had a characteristic synoptic environment (Fig. 5) in which the average melting level (2300 m), IVT (500 kg m s^{-1}), and 925-hPa flow (19 m s^{-1}) were all higher than in any other regime and passed statistical significance testing with the most frequent regime at 95% confidence or greater. The low-level flow direction was generally from the southwest (Fig. 5d), matching the orientation of the Quinault Valley (Fig. 2). The low-level static stability was close to moist neutral with an average N_m^2 of 0.15 (Fig. 5f) although the variance in stability is higher than the other synoptic parameters and it is not significantly different from the most frequent regime. These characteristics are consistent with previously described atmospheric river events. Neiman et al. (2002) found large orographic enhancement when the low-level prefrontal jet was strong and unblocked. The environmental conditions shown in Fig. 5 during the heavy-rain regime support the conclusion of a strong correlation between low-level jet intensity and mountain precipitation made by Neiman et al. (2002). The OLYMPEX observations show that the most pronounced characteristic of the heavy-rain regime is the location of the maximum precipitation enhancement at low to midelevations near the front of the topographic barrier. The higher-elevation sites near the front of the range, Wynoochee and Prairie Creek, averaged 10.7 and 13 mm h^{-1}, respectively, in the heavy-rain regime, far more than Fishery's 5.4 mm h^{-1}. The even-higher elevation SNOTEL site at Buckinghorse (1480 m) recorded less precipitation than Wynoochee in 24 of 27 three-hour heavy-rain periods (not shown).[4] Graves Creek and neighboring interior valley sites also had lower mean precipitation rates in this regime.

An important caveat is that Figs. 4 and 5 examine only the processes that contribute to precipitation at Prairie Creek. However, there were 14 three-hour periods when Wynoochee, at 1020-m elevation compared to 543 m at Prairie Creek, experienced a 5 mm h^{-1} or greater precipitation rate than Prairie Creek. These periods also had above-average IVT, melting levels, and 925-hPa wind speeds. The key difference is that the 925-hPa flow direction was 28° more southerly (179° vs 207°) than the periods of the heavy-rain regime at Prairie Creek. All 14 of these periods were binned in the most frequent distribution at Prairie Creek (section 3a; Fig. 3), meaning there was minimal small-drop production at Prairie Creek. It is plausible that at least some warm rain production occurred on the lower south-facing slopes during these events, but there were no low-elevation disdrometer observations during OLYMPEX on the south side of the Olympic Mountains to confirm this hypothesis.

e. Variations in DSD regime by location

The distributions of (N_w, D_o) in Figs. 3a,b indicate that the four DSD regimes described above occur at different

---

[4] The sample size is 27 instead of 28 in this comparison because of missing precipitation data at Wynoochee.

frequencies at different locations. Table 2 compares the frequency of occurrence and contribution to the total rainfall of each DSD regime at four of the five sites. Over 90% of the 3-h DSDs at Fishery and Graves Creek were categorized as either the "most frequent" category or the "other" category, which contains DSDs that are not classified as any of the four categories. Prairie Creek experienced a far greater variety of DSDs, especially the "heavy rain" category that accounted for 13%–14% of 3-h periods and 31%–34% of the total rainfall at Bishop Field and Prairie Creek, respectively.

The contrast between the two sets of sites indicates that the modulation of precipitating frontal systems by the Olympic Mountains results in both more precipitation and a wider variety of DSDs on and near the lower windward slopes. Figure 7 further illustrates this concept by comparing the overall DSD at Fishery, Bishop Field, and Graves Creek to the overall DSD at Prairie Creek in the different regimes. All time periods classified as a particular regime at Prairie Creek (say lots of small drops; i.e., high N_w and small D_o) were grouped together to obtain a single DSD for the small-drop regime at Prairie Creek. For those same time periods, a single DSD was calculated at each of the other three sites. When Prairie Creek was in the most frequent regime, the other sites had nearly identical DSDs. When Prairie Creek was in other regimes, the DSDs at other sites tended to follow damped versions of the more extreme DSD variations in N_w–D_o coordinate space at Prairie Creek. Both the interior valley site (Graves Creek) and the upstream site (Fishery) tended to remain within the most frequent or other categories (Table 2), whereas Bishop Field had a more similar DSD to Prairie Creek, except when Prairie Creek was in the "large drop" regime. While it is not surprising that similar precipitation growth processes occur at the same times, the degree to which the DSDs are modulated is highly location dependent.

In the next section, results from the 12–13 November event provide further insight into the processes that contribute to the production of intense precipitation at low- to midelevation sites like Bishop Field and Prairie Creek in the heavy-rain regime of southwesterly flow. One aspect of the DSDs that is not evident in the statistics for the whole season in Figs. 3, 4, and 5 is the higher-frequency variability of the DSDs in the heavy-rain regime. The precipitation sometimes shifted toward lower concentrations of larger drops and at other times toward greater concentrations of small- to medium-sized drops. These shifts were sometimes sudden and related to subsynoptic, mesoscale, or embedded convective processes and are described in section 4.

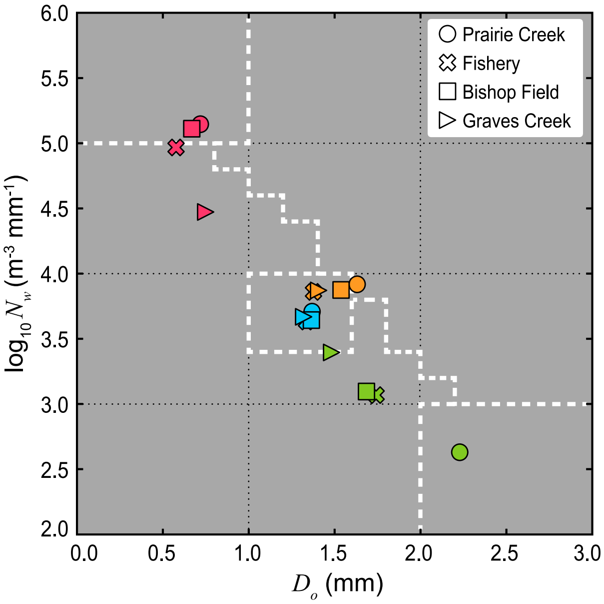

FIG. 7. Scatterplot of the overall D_o vs $\log_{10}(N_w)$ relationship for four of the ground sites. Each point represents the combined DSD for the times that Prairie Creek falls into each of the four DSD regimes. The colors correspond to the regimes in Fig. 6: most frequent (blue), small drops (red), large drops (green), and heavy rain (orange).

4. Case study: 12–13 November 2015

The analysis of 3-hourly DSD statistics for the entire OLYMPEX period has identified large-scale synoptic controls on the DSDs of Pacific storms moving over the Olympic Peninsula. Analysis of the data at higher time resolution reveals sharp and sudden variations of the DSDs on subsynoptic scales. To illustrate this smaller-scale variability, we examine a warm, intense storm that would be considered an atmospheric river that passed over the Olympic Peninsula on the first two days of the OLYMPEX intensive observation period. Figure 8 shows the 36-h precipitation totals from this event. This storm was one of the major precipitation producers during OLYMPEX and caused major flooding of Lake Quinault. In contrast to the seasonal precipitation maximum at Wynoochee (Fig. 2), the greatest amount of precipitation during this event was observed near Lake Quinault at Bishop Field and Prairie Creek. The greatest precipitation occurred on the forward slopes rather than at the highest elevations, which is typical of larger mountain ranges, such as the European Alps (Frei and Schär 1998). Like most Pacific cyclone passages, this storm consisted of several distinct storm sectors (Fig. 1). All four of the DSD regimes described in the previous section were observed. Shifts in DSD regimes often occurred not only when the storm sectors transitioned but also in response to smaller-scale variations of the internal storm structure.

a. *Synoptic overview*

Figure 9 shows NARR reanalysis plots of the melting level and IVT at three times: 2100 UTC 12 November (prefrontal sector), 1200 UTC 13 November (warm sector), and 0000 UTC 14 November (frontal sector). Soundings taken at NPOL and Quillayute (Fig. 2) during the event are shown in a time–height cross section in Fig. 10. Environmental parameters from the NPOL soundings are listed in Table 3. The storm began with passage of a prefrontal sector that lasted from 1200 UTC 12 November to 0300 UTC 13 November at Prairie Creek. The sea level pressure gradient force had an eastward component near the Washington coast (Fig. 9b), and the low-level winds were veering (Fig. 10). The melting level was low compared to the region south of 40°N (Fig. 9a). At sea level, a weak pressure trough separated a colder air mass to the north, and an elongated band of IVT $>400\,\mathrm{kg\,m^{-1}\,s^{-1}}$ stretched for more than 4000 km across the Pacific Ocean (Fig. 9b). A long band of clouds (Fig. 11a) coincided with the IVT band. Cold air remained north of the Olympic Peninsula during the entire event.

The warm sector began at 0300 UTC 13 November when soundings indicated nearly unidirectional flow from the west-southwest and a steady 0°C level just above 2500 m (Fig. 10; Table 3). Cold air was well to the northwest of the Olympic Peninsula, and high IVT impinged directly on the mountains from the west-southwest (Figs. 9c,d). The warm sector was characterized by nearly unchanging large-scale synoptic conditions. However, similar to the coastal storm described by Neiman et al. (2016), smaller-scale waves along the frontal cloud band intermittently enhanced the cloud heights over the warm sector. One such wave appeared around 150°W in Fig. 11a at 2100 UTC 12 November. By 1200 UTC 13 November (Fig. 11b), it was at the coast, and the coldest cloud tops associated with it were over the Olympic Peninsula and slightly offshore. By 1600 UTC 13 November, the wave passed, and the cloud tops were considerably warmer on the coast and just offshore (Fig. 11c).

After the warm sector, the frontal sector spanned the time period 1800–2300 UTC 13 November and includes the passage of a narrow cold-frontal rainband (NCFR) just after 1800 UTC 13 November. This period of precipitation is not considered to be in a postfrontal sector of the type indicated in Fig. 1 because the colder air remained to the northwest of the peninsula until after 0000 UTC 14 November (Figs. 9e,f). The band of IVT had weakened and shifted south, but modest IVT ($>250\,\mathrm{kg\,m^{-1}\,s^{-1}}$) directed toward the windward slopes remained. A sounding launched behind the NCFR at 1802 UTC 13 November (Table 3; Fig. 10) showed that the low-level flow decreased considerably but remained westerly and the melting level remained above 2500 m. By 2300 UTC 13 November, the Quillayute sounding finally shows weak cold advection behind the front (Fig. 10).

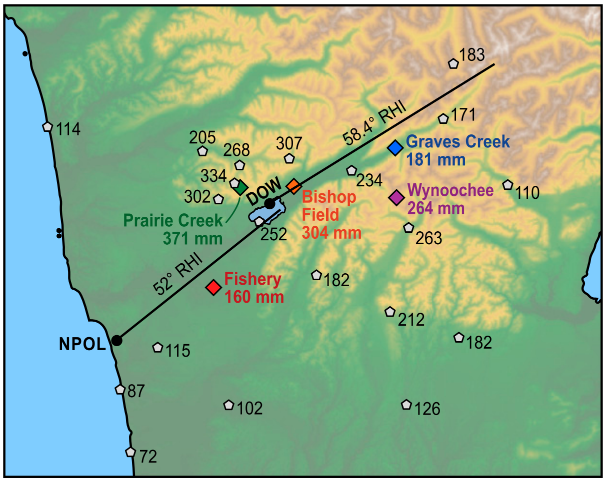

FIG. 8. Precipitation totals for the 12–13 Nov 2015 case study for the sites labeled in Fig. 2 and additional locations from OLYMPEX gauges and other sources including remote automated weather stations (RAWS) and SNOTEL.

b. *Drop size distribution sequence*

For analysis of the 12–13 November 2015 event, the DSDs were calculated in 1-h segments. Figure 12 displays the sequence of 1-h DSDs from Prairie Creek for this case. Three different symbol shapes (circles, diamonds, and triangles) denote the three storm sectors (prefrontal, warm sector, and frontal, respectively). In the early part of the prefrontal period (blue circles), DSDs clustered near the most frequent DSD regime. As synoptic forcing increased with the approaching warm front aloft, the DSD shifted first toward the large-drop regime (low N_w, large D_o) for 3 h and finally into the heavy-rain regime for the last 5 h of the prefrontal sector. The warm sector is divided into two periods, indicated by yellow and red diamonds. Both are within the heavy-rain regime (high N_w and large D_o), which was characterized by melting levels above 2000 m and IVT above $500\,\mathrm{kg\,m^{-1}\,s^{-1}}$ (Fig. 5). During the middle of the warm sector period (1000–1400 UTC 13 November; red diamonds), the DSD shifted toward a contribution from larger drops. The frontal sector (orange triangles) begins with 1 h in the most frequent regime followed by 3 h in the small-drop regime (high N_w and small D_o). These shifts in the DSD are associated with changes in synoptic and mesoscale environmental conditions, which change with storm sectors (Fig. 1) and will be elaborated in the following subsections.

c. *Prefrontal period (1200 UTC 12 November–0300 UTC 13 November)*

The prefrontal sector for this case had characteristics consistent with descriptions of the early sector or

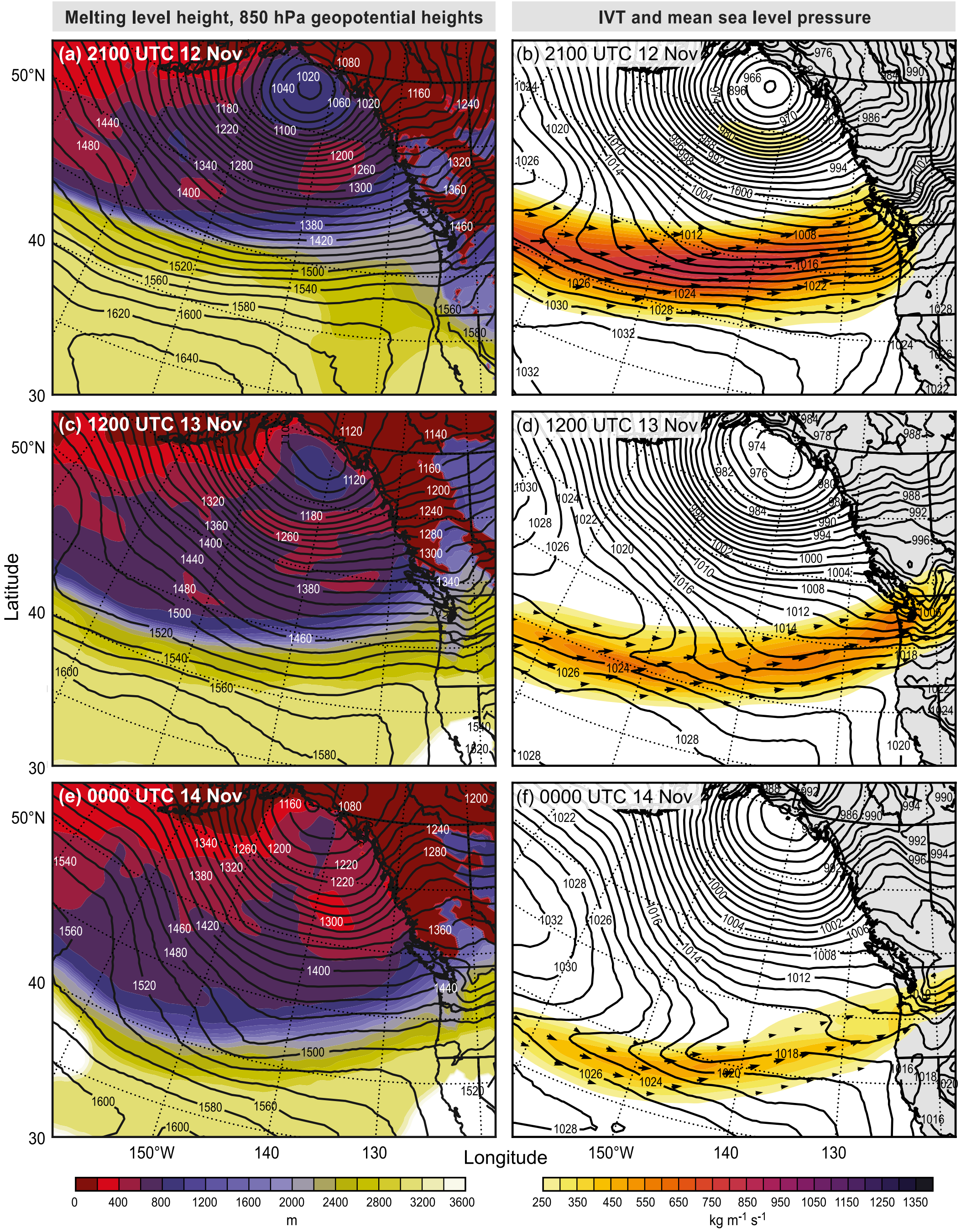

FIG. 9. NARR maps showing the synoptic setup of the 12–13 Nov 2015 case study at three times: (a),(b) 2100 UTC 12 Nov, (c),(d) 1200 UTC 13 Nov, and (e),(f) 0000 UTC 14 Nov 2015. (a),(c),(e) Melting-level height (colors) and 850-hPa geopotential heights (contours); (b),(d),(f) integrated vapor transport (colors and vectors) and sea level pressure (contours).

pre-warm-frontal passages in prior studies (Locatelli and Hobbs 1987; Medina et al. 2007). During the passage of this sector, southerly component winds at low levels veered with height, and the melting level rose significantly, as indicated by the soundings launched from the NPOL site at 1458, 1805, and 2110 UTC 12 November (Fig. 10; Table 3). The 30-min rain rates at the five ground sites shown in Fig. 13a gradually increased with similar rates at all sites prior to 2200 UTC 12 November. To illustrate the small-scale variability of the DSD

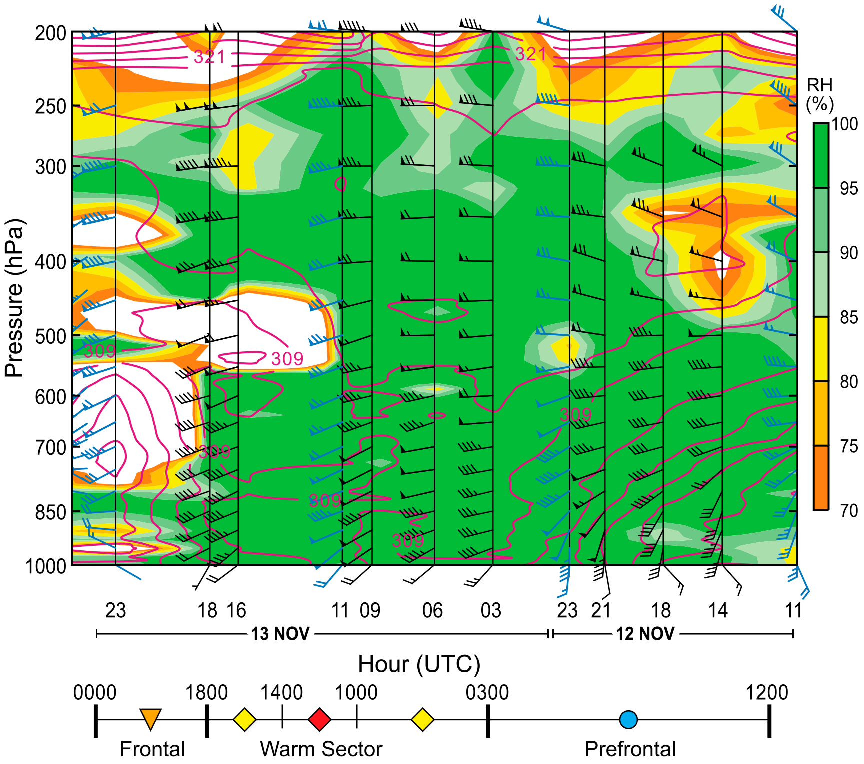

FIG. 10. Time–height cross section of soundings launched during the 12–13 Nov 2015 case study. Black lines and wind barbs (kt; 1 kt = 0.51 m s^{-1}) denote soundings launched from NPOL. Blue lines and wind barbs (kt) denote soundings launched from Quillayute (Fig. 2). Red contours denote potential temperature θ. Colored contours denote relative humidity (%). Figure provided by Paul Ciesielski.

during the 12–13 November storm, the DSDs at Prairie Creek are calculated at 5-min resolution (Figs. 13b,c). During the passage of the prefrontal sector, these DSDs consisted of small quantities of both larger and smaller drops, especially prior to 1900 UTC 12 November (Fig. 13b). Figure 13c shows the contribution to the rain rate from each of the Prairie Creek PARSIVEL drop size bins, with the total bar representing the 5-min rain rate estimated by the PARSIVEL. The light precipitation rates, weak orographic enhancement, and low concentrations of both small and large drops prior to 1900 UTC were all characteristics of the most frequent DSD regime (section 3a). During the period from 1900 to 2200 UTC 12 November, the DSD briefly shifted toward the large-drop (low N_w and large D_o) regime. Figure 13c shows that most of the rainfall came from the larger drops (yellow-brown colors) during this 3-h period, but the overall rain rate remained below 8 mm h^{-1} at all five stations (Fig. 13a). This period is consistent with the lack of precipitation enhancement described for the large-drop (low N_w and high D_o) regime (section 3c; Fig. 4).

A sudden large change in the prefrontal DSD occurred at 2200 UTC 12 November when the DSD shifted to the high N_w, large D_o heavy-rain regime and remained in that

TABLE 3. Synoptic environmental parameters computed from the eight soundings launched at NPOL during the 12–13 Nov 2015 event.

Time	0°C level (m)	IVT (kg m^{-1} s^{-1})	925-hPa speed (m s^{-1})	925-hPa direction (°)	950–850-hPa N_d^2 ($\times10^4$)	950–850-hPa N_m^2 ($\times10^4$)
1458 UTC 12 Nov	1334	337	18.3	205	1.24	0.05
1805 UTC 12 Nov	1520	427	18.6	207	1.38	0.15
2110 UTC 12 Nov	2219	610	25.5	191	2.03	0.78
0305 UTC 13 Nov	2584	637	21.7	253	1.56	0.12
0610 UTC 13 Nov	2680	693	22.5	246	1.51	0.08
0928 UTC 13 Nov	2560	716	27.5	239	1.61	0.20
1632 UTC 13 Nov	2582	573	22.1	240	1.62	0.19
1802 UTC 13 Nov	2512	496	13.8	248	1.97	0.58

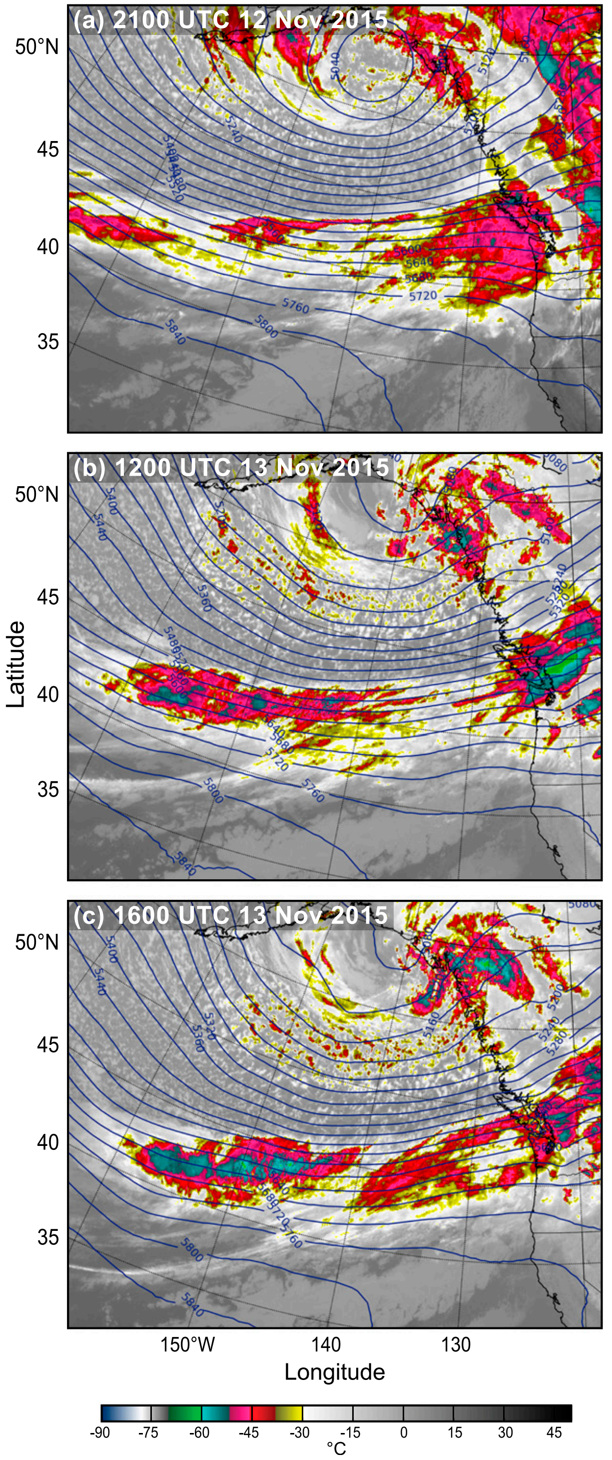

FIG. 11. GOES-West infrared imagery and NARR 500-hPa geopotential heights (contours) for (a) 2100 UTC 12 Nov, (b) 1200 UTC 13 Nov, and (c) 1600 UTC 13 Nov 2015.

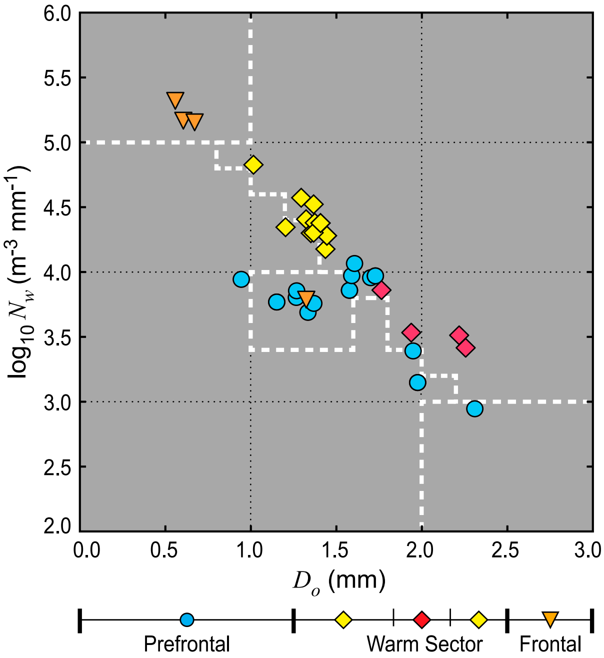

FIG. 12. Scatterplot of the D_o vs $\log_{10}(N_w)$ relationship for 1-h periods at Prairie Creek during the 12–13 Nov 2015 case study. Symbol shapes denote the prefrontal (circles), warm sector (diamonds), and frontal (triangles) periods. Symbol colors denote the four major periods described in the text.

state for the remainder of the passage of the prefrontal sector (2200 UTC 12 November to 0300 UTC 13 November; cluster of blue circles in the heavy-rain regime in Fig. 12). This change is probably related to the increase of low-level flow associated with the arriving warm front. During this period, the melting level rose 400 m to nearly 2600 m, and the 925-hPa wind direction shifted to the southwest (Table 3). The Prairie Creek DSD shows high concentrations of drops of all sizes during this time period with a rapid increase in numbers of small drops (Fig. 13b). During this time period, the precipitation rate at Prairie Creek (and to a lesser extent Bishop Field) increased to over 20 mm h^{-1}, while other sites remained below 10 mm h^{-1} (Fig. 13a). This increase in rain rate was mostly accounted for by the increase of small- to medium-sized drops (<2 mm), and by 0200 UTC 13 November, these smaller drops contributed up to over two-thirds of the total 20 mm h^{-1} rain rate at Prairie Creek (Fig. 13c). The spike in precipitation rate at Wynoochee around 2200 UTC 12 November should be disregarded; it was caused by a chunk of snow dropping from the rim of the Pluvio into the bucket.

A vertical cross section obtained by combining NPOL and DOW radar data from this period at 2152 UTC 12 November shows several key features that help to understand the DSD variations during the passage of the prefrontal sector. The cross section (black line in Figs. 2 and 8) bisects the Quinault Valley to best view near-surface features and avoid low-level beam blockage near Prairie Creek. The reflectivity field in Fig. 14a

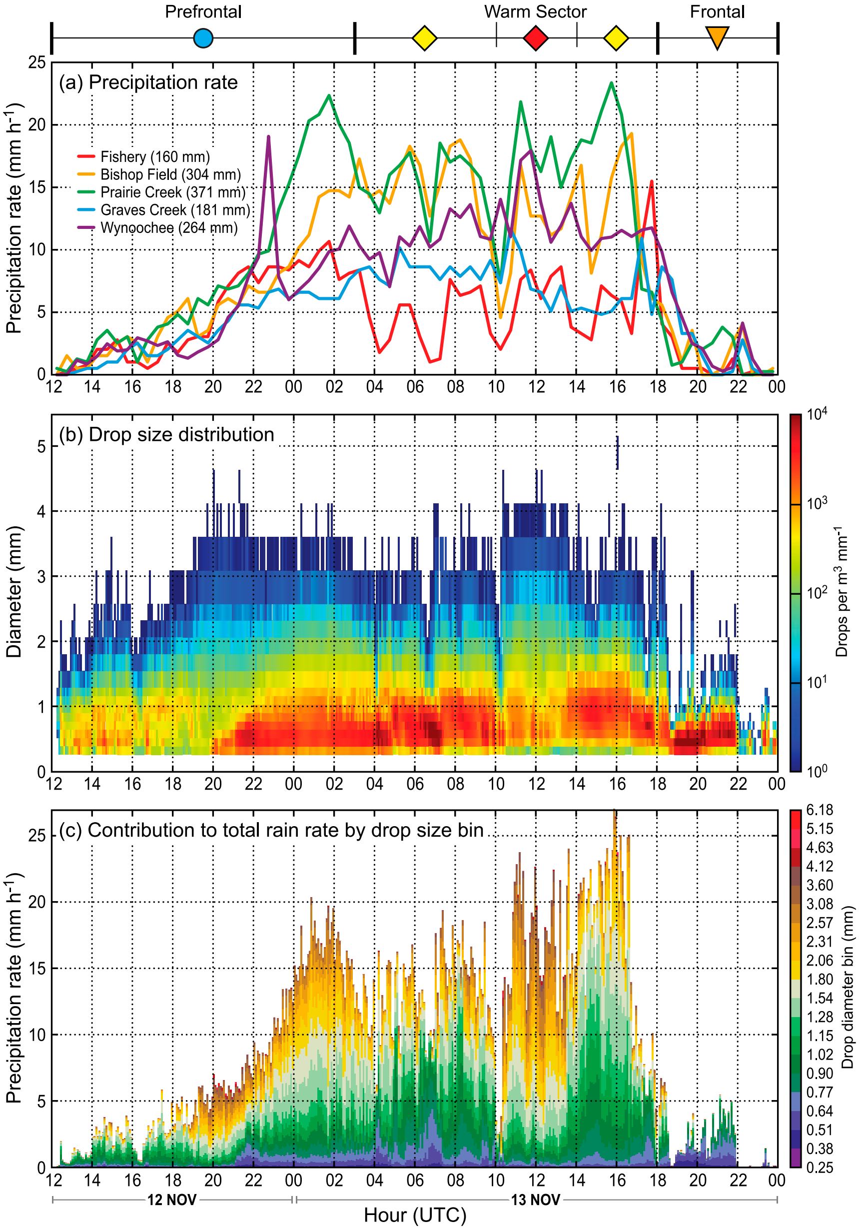

FIG. 13. Time series of ground instrument data during the 12–13 Nov 2015 case study. The symbols at the top match the time periods diagrammed in Fig. 10. (a) The 30-min precipitation rate at the five ground sites. (b) The 5-min Prairie Creek DSD. (c) The 5-min contribution to the total rain rate by PARSIVEL drop size bin at Prairie Creek. The spike in precipitation rate at Wynoochee in (a) at 2230 UTC 12 Nov was caused by a chunk of snow dropping into the Pluvio bucket.

indicates a relatively deep layer of ice particles above the bright band and nearly uniform reflectivity below the bright band.[5] An onshore-directed low-level jet exceeding 24 m s^{-1} in radial velocity (Fig. 14b) rose from around 1–1.5 km above the surface near the coast to 2–3 km above the surface ~50 km inland. The radial velocity was directed toward the radars (down valley) below 1 km in the Quinault Valley (Fig. 9). Two distinct processes may have contributed to the increased concentration of larger (>2-mm drops) at Prairie Creek during this period (Fig. 13b). The presence of enhanced

---

[5] The bright band is located at a lower elevation in the Quinault Valley because residual cold air was trapped in the valley and/or the processes described in Minder et al. (2011).

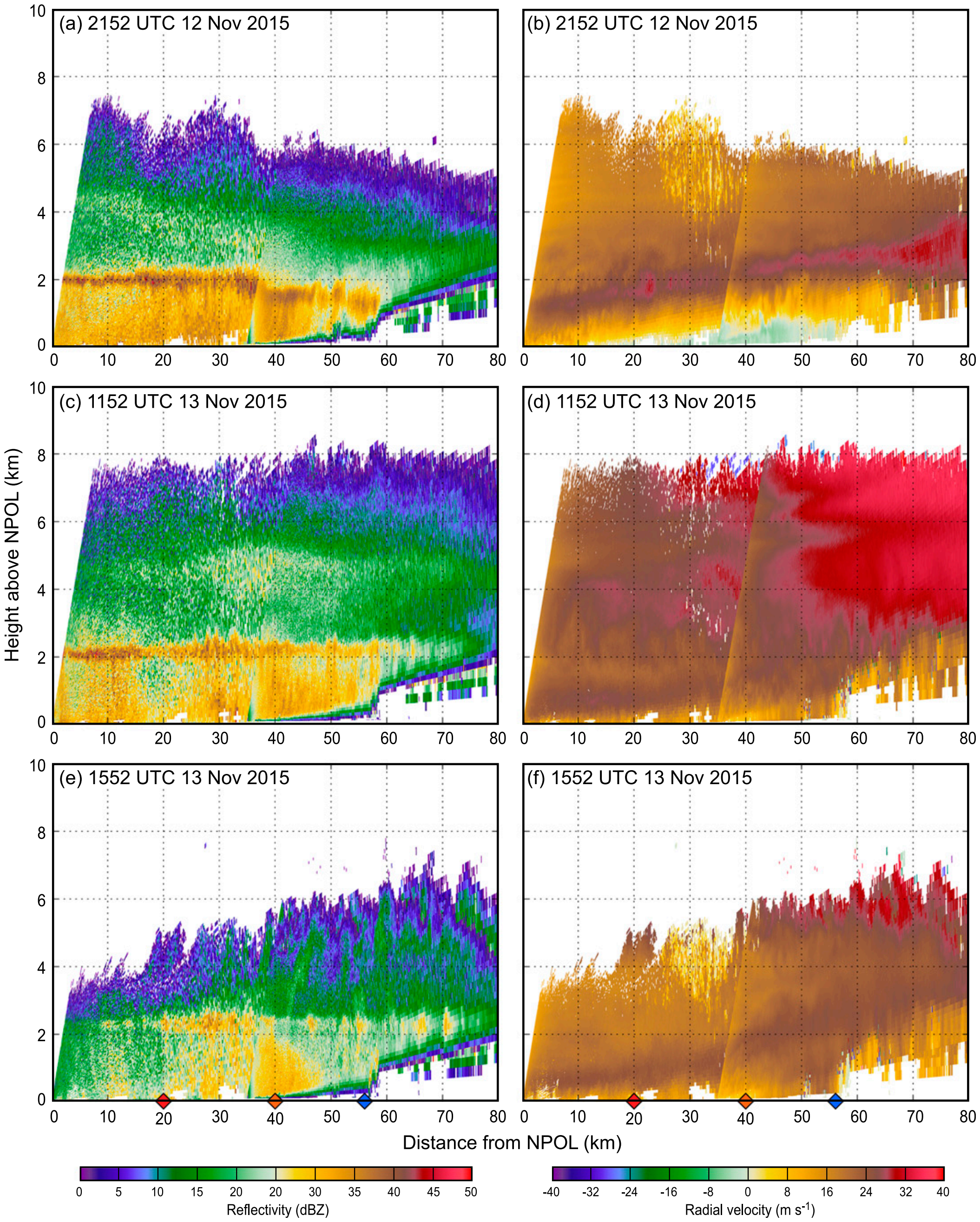

FIG. 14. Combined NPOL–DOW cross-sectional images of (a),(c),(e) reflectivity and (b),(d),(f) radial velocity for (top) 2152 UTC 12 Nov and (middle) 1152 and (bottom) 1552 UTC 13 November. The location of the cross section is shown in Figs. 2 and 8. The NPOL was 139 m above sea level. The diamonds on the *x* axis indicate the location of three ground sites along the cross section: Fishery (red diamond; 20 km from NPOL), Bishop Field (orange diamond; 40 km from NPOL), and Graves Creek (blue diamond; 58 km from NPOL). The DOW was 35 km from NPOL. The Python ARM Radar Toolkit (Py-ART) module (Helmus and Collis 2016) provided software for radar plotting.

reflectivity above the bright band (3–5-km elevation) indicates robust growth of ice particles at those altitudes either due to orographic lifting of the air at mid–upper levels or, possibly, shear-generated turbulence over the Quinault Valley. The latter was indicated by increased Doppler spectrum width (not pictured), which could have been enhancing hydrometeor growth [as suggested by Houze and Medina (2005) and Medina and Houze (2015)].

d. Warm sector (0300–1800 UTC 13 November)

After the passage of the prefrontal sector, the 0°C level rose, and the low-level easterly toward-radar flow was replaced by southwesterly onshore and upslope flow. As a result, the shear-induced turbulence decreased (not shown), and the low-level flow lifting became focused directly over the low- to midelevation windward slopes and below the bright band. The warm sector passage began at about 0300 UTC 13 November, when the low-level temperature advection ended and the wind direction became nearly uniform with height from the west-southwest (Fig. 10). The synoptic environment was generally uniform throughout the 15-h warm sector. During this time, the 0°C level was 2600 ± 80 m, the 925-hPa wind speed was 24 ± 4 m s^{-1} and the 925-hPa wind direction was 246° ± 7° (see soundings from 0305, 0610, 0928, and 1632 UTC in Table 3 and Fig. 10). The high melting level and strong low-level moisture advection from the west-southwest closely matches the synoptic environment described in Fig. 5 for the high N_w and large D_o heavy-rain regime.

Figure 12 shows that all 15 h of the warm sector passage fell along or to the right of the stair-step diagonal line, corresponding to the DSDs associated with the heaviest rain of OLYMPEX. Most of the warm sector had large quantities of small- to medium-sized drops contributing to the majority of the rain rate. However, during the 1000–1400 UTC 13 November period, the concentration of drops less than 1 mm decreased while drops greater than 2 mm reached the highest concentrations of the entire event (Figs. 13b,c). Yet the rain rate at Prairie Creek underwent only a modest increase during the large-drop period, from 15 mm h^{-1} (0300–1000 UTC 13 November) to 17 mm h^{-1} (1000–1400 UTC 13 November). After 1400 UTC 13 November, the rain rate increased further, up to 23 mm h^{-1}, when the DSDs switched back to favoring small- to medium-sized drops.

Figures 14c,d (1152 UTC 13 November) correspond to the larger-drop-dominated period (red diamonds in Fig. 12). During this period, the vertical cross section at 1152 UTC shows echo tops up to 8 km, a strong bright band at 2 km, and a secondary maximum in reflectivity above the melting level at 4 km (Fig. 13c). This period coincides with the subsynoptic-scale wave perturbation discussed earlier, which was manifested by high cloud tops in the infrared satellite image in Fig. 11b (section 4a). The deep ice layer and secondary reflectivity maximum aloft indicate that ice processes were important for precipitation growth during this period. The dynamical reason for the enhancement could have been vertical motion enhancement by a wave on the front or some other mesoscale vertical motion perturbation superimposed on the synoptic-scale storm system. From a microphysical standpoint, the large drops observed by the PARSIVEL during this time likely were formed by the melting of large aggregate snowflakes formed above the bright band and grew by collecting smaller drops formed below the bright band.

Figures 14e,f (1552 UTC 13 November) correspond to the period dominated by smaller drops (yellow diamonds in Fig. 12). During this period, the DOW–NPOL RHI taken at 1552 UTC shows that the bright band was above 2 km but weaker and echoes reached up to only ~4 km over the coast and ~6 km over the mountains 60 km east of NPOL. The infrared satellite image also shows a shallower cloud field at this time (Fig. 11c), and the sounding cross section shows drying from 550 to 450 hPa (Fig. 10). Nevertheless, both velocity fields show a low-level jet (of 20–15 m s^{-1}) lifting from below 1 km near the coast up to 3–4 km over the mountains, especially during the later time period (Figs. 14d,f). The low-level easterly flow and adjacent shear layer were not present in the warm sector. The lifting of the jet from below the bright band in the warm layer during the warm sector evidently provided the mechanism for rapid growth of small droplets through the processes of condensation and collision–coalescence.

e. Frontal period (1800 UTC 13 November–0000 UTC 14 November)

An NCFR passage around 1800 UTC 13 November lasted about 5 min at Prairie Creek and therefore had negligible impact on the 1-h accumulated DSDs. An NPOL sounding taken just after the NCFR passage (1805 UTC) indicated that the 0°C level was at 2.5 km and 925-hPa winds were 14 m s^{-1} from 250°. The Olympic Peninsula remained within warm, moist westerly component flow behind the cold front, although there was a significant decrease in low-level flow speed, IVT, and the depth of the moist layer (Table 3; Fig. 10). Steady precipitation continued at Prairie Creek through 2200 UTC 13 November. The DSD in Fig. 12 was within the high N_w, small D_o small-drop regime for 3 h (1900–2200 UTC 13 November). The Prairie Creek DSD (Fig. 13b) had high concentrations of drops <1 mm during this period and few if any drops >1 mm. Despite their large number concentration, these small-sized drops resulted in a low rain rate of <5 mm h^{-1}. During this period, the DSD (Figs. 12 and 13b) closely matched the example of nonbrightband rain in Martner et al. (2008). In the 12–13 November case, this small-drop regime was not a significant contributor to the rainfall totals, although it could be significant in warm, weakly forced events of long duration.

5. Conclusions

Statistics of the DSDs observed in all stratiform precipitation that occurred during the season-long OLYMPEX field campaign and a case study of one strong storm have yielded the following conclusions:

- Four precipitation regimes are defined from the DSDs:
  - Most frequently occurring: Moderate N_w and D_o
  - Less frequent: High concentrations of small drops, high N_w, and small D_o
  - Less frequent: Low concentrations of big drops, low N_w, and large D_o
  - Heaviest-rain periods: High N_w and large D_o
- The most frequent DSD regime is associated with seasonally average synoptic conditions. Orographic precipitation enhancement is modest and predominates at higher elevations.
- The heaviest-rain regime had high melting level, large IVT, nearly moist neutral stability, and strong low-level flow from the west-southwest, allowing for unimpeded lift of the flow over the topographic barrier and production of the largest rain rates at low to midelevations near the front of the barrier.
- Analysis of a heavy precipitation case shows how the DSD varies with synoptic storm sectors and changes abruptly during the passage of embedded subsynoptic structures.

Different modes of precipitation enhancement on the lower windward slopes are summarized in Fig. 15. This visual aid is guided by both the full cold-season statistics (section 3) and the case study (section 4). It is also consistent with several other heavy-rain-producing cases in OLYMPEX (e.g., 16–17 November and 8–9 December 2015). Figure 15a closely corresponds to the most frequent DSD regime (section 3a) and the early part of the prefrontal period of the case study (section 4c). It shows a relatively deep stratiform cloud layer with primary precipitation production in the ice layer above the melting level. Relatively small concentrations of larger drops fall into a lower layer that comes from either a southerly or offshore direction that does not impinge directly on the Olympic Mountains barrier. There is modest enhancement of precipitation on the low- to midelevation windward slopes because there is minimal generation of cloud water or small raindrops at low elevations. The DSDs are similar at all locations (Fig. 7). Modest precipitation enhancement at higher windward elevations can occur, possibly because of midlevel flow lifting over the mountains above the lower layer.

Figure 15b fits closely with the heavy-rain DSD regime (section 3d) and the warm sector period of the case study (section 4d). During heavy-rain periods, onshore-directed low-level flow lifts unimpeded over the low-elevation mountain slopes. Large quantities of small drops are formed by condensation and collision–coalescence above the low- to midelevation windward slopes. Ice-initiated drops fall from a high 0°C level and collect some of the small drops, consistent with the process suggested by Minder et al. (2008). Deep precipitating clouds with considerable ice production are not necessary to generate heavy rainfall on the windward slopes but can be responsible for shifts toward smaller concentrations of larger drops. Lifting of the warm, moist neutral low-level jet is the dominant precipitation-generating process throughout the heavy-rain regime. The case study analysis in section 4 illustrates how there can be rapid shifts in the scenarios illustrated in Figs. 15a,b within one storm that depend on storm sector and subsynoptic-scale variability.

The importance of warm rain processes in west-coastal orographic environments was also noted in California (White et al. 2003; Kingsmill et al. 2006; Martner et al. 2008; Kingsmill et al. 2016) and in the Nahuelbuta Range in Chile (Massmann et al. 2017). The California studies took the approach of classifying the dominant microphysical process by using the presence of a bright band in vertically pointing radar observations. This separation is effective at isolating instances of shallow warm rain with little if any contribution from melting ice. However, it does not account for the considerable variability in precipitation microphysics that occurs when a bright band is present. During stratiform raining periods in OLYMPEX, a bright band was evident on vertically pointing radar over 90% of the time (Table 2), including periods when warm rain processes were clearly dominant (see Figs. 13 and 14). However, even during those periods, ice processes were still contributing to precipitation growth. This study demonstrates that the precipitation over the Olympic Mountains is a complex mix of warm low-level growth and ice-originated rainfall where their relative importance is modulated by synoptic and mesoscale conditions. Future studies will employ other OLYMPEX datasets such as the dual-polarization radar data, microphysical sampling from aircraft, and high-resolution modeling to further explore these precipitation processes and their modulation by synoptic environment and complex terrain.

We further note that this study has implications regarding the convective–stratiform partitioning used to characterize rainfall variability in deep convective regimes. The heavy rain and large quantities of small-drops regimes described above in sections 3b and 3d fall in the same N_w–D_o space that has been associated with convective radar echoes in the tropics (Bringi et al. 2009;

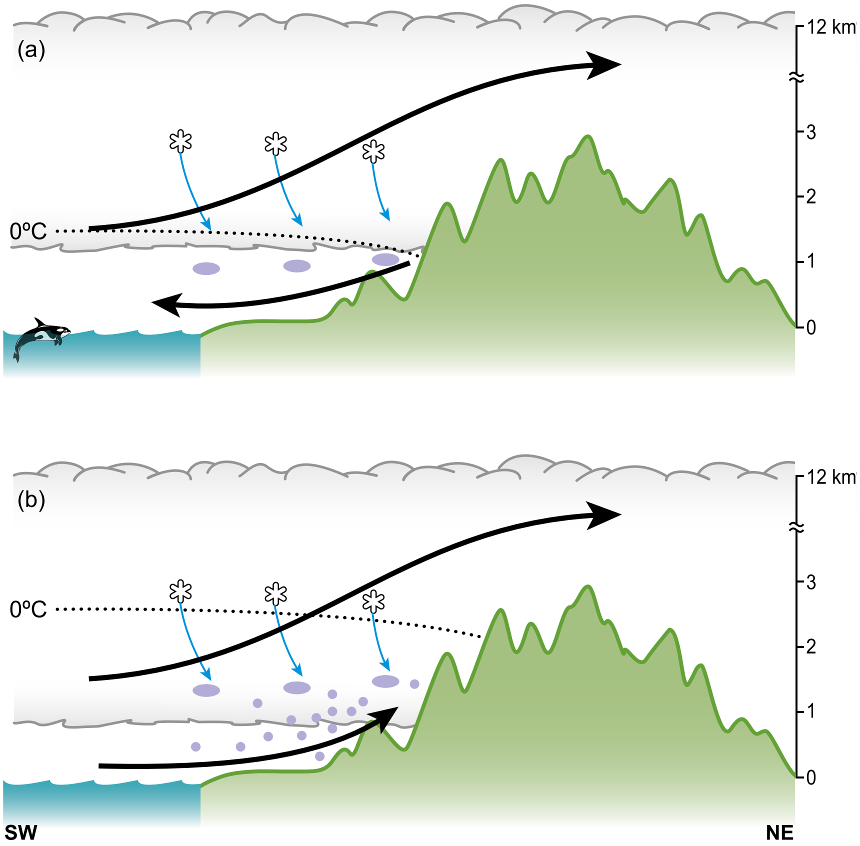

FIG. 15. Visual aid depicting the typical flow and precipitating cloud structure as extratropical cyclones move from the Olympic Coast National Marine Sanctuary to the Olympic Mountains for (a) minimal precipitation enhancement on the lower windward slopes and (b) considerable enhancement of precipitation on the lower windward slopes. The NASA ER-2 aircraft provided cloud-top height estimates. Terminal aerodrome forecasts (TAFs) from Hoquiam, Washington (Fig. 2), provided cloud-base estimates. Black arrows represent the low- and midlevel flow directions. Ellipses represent large raindrops formed from melted ice particles. Circles represent small raindrops formed by condensation and collision–coalescence.

Thompson et al. 2015). However, this study is restricted to stratiform precipitation, demonstrating that both convective and stratiform precipitation can exhibit the same DSDs. We therefore conclude that DSDs alone cannot in general be used to describe whether precipitation resulted from convective or stratiform processes.

A primary goal of OLYMPEX was to provide physical ground validation for the GPM satellite. Spaceborne radar retrievals require a parameterized DSD to convert reflectivity to rain rate (Iguchi and Meneghini 1994), a difficult problem given the complexities of stratiform DSDs observed in this study. Subsynoptic-scale perturbations (e.g., 1000–1400 UTC 12 November 2015) can modify the vertical cloud structure and DSD without appreciably changing the underlying rain rate. Ground clutter removal algorithms must preserve as much near-surface information as possible to capture the below-brightband warm rain processes. Warm precipitation processes also present challenges for passive microwave retrievals of precipitation over land since the precipitation estimates are somewhat biased toward the mean rain rate associated with a given ice-scattering signature (Kummerow et al. 2011, 2015).

Acknowledgments. The authors thank M. Wingo, B. Baccus, C. Urnes, A. Hart, N. Johnson, S. Domokos, H. Mohrmann, B. Jameson, B. Gilles, and J. Nowak for making major contributions to deployment and maintenance of the ground sites used in this study. The authors would also like to thank the Olympic National Park, the U. S. Forest Service, and the Quinault Indian Nation for permission to install instrumentation on their land. A. Tokay, P. Gatlin, and D. Wolff helped process and interpret disdrometer data. Dr. Paul Ciesielski provided the sounding cross section. Beth Tully provided graphics and editing support. Comments by three anonymous reviewers considerably strengthened the manuscript. This research was supported by NASA Grants NNX15AL38G, NNX16AK05G, and NNX16AD75G and NSF Grants AGS-1503155 and AGS-1657251.

REFERENCES

Atlas, D., R. C. Srivastava, and R. S. Sekhon, 1973: Doppler radar characteristics of precipitation at vertical incidence. *Rev. Geophys.*, **11**, 1–35, https://doi.org/10.1029/RG011i001p00001.

Barrett, B. S., R. Garreaud, and M. Falvey, 2009: Effect of the Andes Cordillera on precipitation from a midlatitude cold front. *Mon. Wea. Rev.*, **137**, 3092–3109, https://doi.org/10.1175/2009MWR2881.1.

Bond, N. A., and Coauthors, 1997: The Coastal Observation and Simulation with Topography (COAST) experiment. *Bull. Amer. Meteor. Soc.*, **78**, 1941–1955, https://doi.org/10.1175/1520-0477(1997)078<1941:TCOASW>2.0.CO;2.

Bringi, V. N., G.-J. Huang, V. Chandrasekar, and E. Gorgucci, 2002: A methodology for estimating the parameters of a gamma raindrop size distribution model from polarimetric radar data: Application to a squall-line event from the TRMM/Brazil campaign. *J. Atmos. Oceanic Technol.*, **19**, 633–645, https://doi.org/10.1175/1520-0426(2002)019<0633:AMFETP>2.0.CO;2.

——, C. R. Williams, M. Thurai, and P. T. May, 2009: Using dual-polarized radar and dual-frequency profiler for DSD characterization: A case study from Darwin, Australia. *J. Atmos. Oceanic Technol.*, **26**, 2107–2122, https://doi.org/10.1175/2009JTECHA1258.1.

Durran, D. R., and J. B. Klemp, 1982: On the effects of moisture on the Brunt–Väisälä frequency. *J. Atmos. Sci.*, **39**, 2152–2158, https://doi.org/10.1175/1520-0469(1982)039<2152:OTEOMO>2.0.CO;2.

Frei, C., and C. Schär, 1998: A precipitation climatology of the Alps from high-resolution rain-gauge observations. *Int. J. Climatol.*, **18**, 873–900, https://doi.org/10.1002/(SICI)1097-0088(19980630)18:8<873::AID-JOC255>3.0.CO;2-9.

Garreaud, R., M. Falvey, and A. Montecinos, 2016: Orographic precipitation in coastal southern Chile: Mean distribution, temporal variability, and linear contribution. *J. Hydrometeor.*, **17**, 1185–1202, https://doi.org/10.1175/JHM-D-15-0170.1.

Helmus, J., and S. Collis, 2016: The Python ARM Radar Toolkit (Py-ART), a library for working with weather radar data in the Python programming language. *J. Open Res. Software*, **4**, p.e25, https://doi.org/10.5334/jors.119.

Hobbs, P. V., 1978: Organization and structure of clouds and precipitation on the mesoscale and microscale in cyclonic storms. *Rev. Geophys.*, **16**, 741–755, https://doi.org/10.1029/RG016i004p00741.

——, and Coauthors, 1971: Studies of winter cyclonic storms over the Cascade Mountains (1970–71). University of Washington Dept. of Atmospheric Sciences Cloud Physics Group Research Rep. VI, 306 pp., http://carg.atmos.washington.edu/sys/research/archive/winter_cyclonic.pdf.

Houze, R. A., Jr., and S. Medina, 2005: Turbulence as a mechanism for orographic precipitation enhancement. *J. Atmos. Sci.*, **62**, 3599–3623, https://doi.org/10.1175/JAS3555.1.

——, J. D. Locatelli, and P. V. Hobbs, 1976: Dynamics and cloud microphysics of the rainbands in an occluded frontal system. *J. Atmos. Sci.*, **33**, 1921–1936, https://doi.org/10.1175/1520-0469(1976)033<1921:DACMOT>2.0.CO;2.

——, and Coauthors, 2017: The Olympic Mountains Experiment (OLYMPEX). *Bull. Amer. Meteor. Soc.*, **98**, 2167–2188, https://doi.org/10.1175/BAMS-D-16-0182.1.

Iguchi, T., and R. Meneghini, 1994: Intercomparison of single-frequency methods for retrieving a vertical rain profile from airborne or spaceborne radar data. *J. Atmos. Oceanic Technol.*, **11**, 1507–1516, https://doi.org/10.1175/1520-0426(1994)011<1507:IOSFMF>2.0.CO;2.

Kingsmill, D. E., P. J. Neiman, F. M. Ralph, and A. B. White, 2006: Synoptic and topographic variability of Northern California precipitation characteristics in landfalling winter storms observed during CALJET. *Mon. Wea. Rev.*, **134**, 2072–2094, https://doi.org/10.1175/MWR3166.1.

——, ——, and A. B. White, 2016: Microphysics regime impacts on the relationship between orographic rain and orographic forcing in the coastal mountains of Northern California. *J. Hydrometeor.*, **17**, 2905–2922, https://doi.org/10.1175/JHM-D-16-0103.1.

Kummerow, C. D., S. Ringerud, J. Crook, D. Randel, and W. Berg, 2011: An observationally generated a priori database for microwave rainfall retrievals. *J. Atmos. Oceanic Technol.*, **28**, 113–130, https://doi.org/10.1175/2010JTECHA1468.1.

——, D. L. Randel, M. Kulie, N.-Y. Wang, R. Ferraro, S. J. Munchak, and V. Petkovic, 2015: The evolution of the Goddard profiling algorithm to a fully parametric scheme. *J. Atmos. Oceanic Technol.*, **32**, 2265–2280, https://doi.org/10.1175/JTECH-D-15-0039.1.

Locatelli, J. D., and P. V. Hobbs, 1987: The mesoscale and microscale structure and organization of clouds and precipitation in midlatitude cyclones. XIII: Structure of a warm front. *J. Atmos. Sci.*, **44**, 2290–2309, https://doi.org/10.1175/1520-0469(1987)044<2290:TMAMSA>2.0.CO;2.

Martner, B. E., S. E. Yuter, A. B. White, S. Y. Matrosov, D. E. Kingsmill, and F. M. Ralph, 2008: Raindrop size distributions and rain characteristics in California coastal rainfall for periods with and without a radar bright band. *J. Hydrometeor.*, **9**, 408–425, https://doi.org/10.1175/2007JHM924.1.

Massmann, A. K., J. R. Minder, R. D. Garreaud, D. E. Kingsmill, R. A. Valenzuela, A. Montecinos, S. L. Fults, and J. R. Snider, 2017: The Chilean Coastal Orographic Precipitation Experiment: Observing the influence of microphysical rain regimes on coastal orographic precipitation. *J. Hydrometeor.*, **18**, 2723–2743, https://doi.org/10.1175/JHM-D-17-0005.1.

Matejka, T. J., R. A. Houze, and P. V. Hobbs, 1980: Microphysics and dynamics of clouds associated with mesoscale rainbands in extratropical cyclones. *Quart. J. Roy. Meteor. Soc.*, **106**, 29–56, https://doi.org/10.1002/qj.49710644704.

Medina, S., and R. A. Houze Jr., 2015: Small-scale precipitation elements in midlatitude cyclones crossing the California Sierra Nevada. *Mon. Wea. Rev.*, **143**, 2842–2870, https://doi.org/10.1175/MWR-D-14-00124.1.

——, E. Sukovich, and R. A. Houze Jr., 2007: Vertical structures of precipitation in cyclones crossing the Oregon Cascades. *Mon. Wea. Rev.*, **135**, 3565–3586, https://doi.org/10.1175/MWR3470.1.

Mesinger, F., and Coauthors, 2006: North American Regional Reanalysis. *Bull. Amer. Meteor. Soc.*, **87**, 343–360, https://doi.org/10.1175/BAMS-87-3-343.

Minder, J. R., D. R. Durran, G. H. Roe, and A. M. Anders, 2008: The climatology of small-scale orographic precipitation over the Olympic Mountains: Patterns and processes. *Quart. J. Roy. Meteor. Soc.*, **134**, 817–839, https://doi.org/10.1002/qj.258.

——, ——, and ——, 2011: Mesoscale controls on the mountainside snow line. *J. Atmos. Sci.*, **68**, 2107–2127, https://doi.org/10.1175/JAS-D-10-05006.1.

Nagle, R. E., and S. M. Serebreny, 1962: Radar precipitation echo and satellite cloud observations of a maritime cyclone. *J. Appl. Meteor.*, **1**, 279–295, https://doi.org/10.1175/1520-0450(1962)001<0279:RPEASC>2.0.CO;2.

Neiman, P. J., F. M. Ralph, A. B. White, D. E. Kingsmill, and P. O. G. Persson, 2002: The statistical relationship between upslope flow and rainfall in California's coastal mountains: Observations during CALJET. *Mon. Wea. Rev.*, **130**, 1468–1492, https://doi.org/10.1175/1520-0493(2002)130<1468:TSRBUF>2.0.CO;2.

——, ——, G. A. Wick, J. D. Lundquist, and M. D. Dettinger, 2008: Meteorological characteristics and overland precipitation impacts of atmospheric rivers affecting the west coast of North America based on eight years of SSM/I satellite observations. *J. Hydrometeor.*, **9**, 22–47, https://doi.org/10.1175/2007JHM855.1.

——, B. J. Moore, A. B. White, G. A. Wick, J. Aikins, D. L. Jackson, J. R. Spackman, and F. M. Ralph, 2016: An airborne and ground-based study of a long-lived and intense atmospheric river with mesoscale frontal waves impacting California during CalWater-2014. *Mon. Wea. Rev.*, **144**, 1115–1144, https://doi.org/10.1175/MWR-D-15-0319.1.

Nešpor, V., and B. Sevruk, 1999: Estimation of wind-induced error of rainfall gauge measurements using a numerical simulation. *J. Atmos. Oceanic Technol.*, **16**, 450–464, https://doi.org/10.1175/1520-0426(1999)016<0450:EOWIEO>2.0.CO;2.

Newell, R. E., N. E. Newell, Y. Zhu, and C. Scott, 1992: Tropospheric rivers?—A pilot study. *Geophys. Res. Lett.*, **19**, 2401–2404, https://doi.org/10.1029/92GL02916.

NOAA/OAR/ESRL PSD, 2004: North American Regional Reanalysis data from NCEP global reanalysis. NOAA/OAR/ESRL PSD, accessed 24 August 2016, https://www.esrl.noaa.gov/psd/data/gridded/data.narr.html.

Petersen, W., and Coauthors, 2017: Olympic Mountain Experiment (OLYMPEX) for GPM ground validation collection. NASA Global Hydrology Resource Center Distributed Active Archive Center, accessed 26 September 2016, https://ghrc.nsstc.nasa.gov/home/content/olympex-datasets-currently-release.

Ralph, F. M., and Coauthors, 1999: The California Land-falling Jets Experiment (CALJET): Objectives and design of a coastal atmosphere–ocean observing system deployed during a strong El Niño. Preprints, *Third Symp. on Integrated Observing Systems,* Dallas, TX, Amer. Meteor. Soc., 78–81.

——, P. J. Neiman, and G. A. Wick, 2004: Satellite and CALJET aircraft observations of atmospheric rivers over the eastern North Pacific Ocean during the winter of 1997/98. *Mon. Wea. Rev.*, **132**, 1721–1745, https://doi.org/10.1175/1520-0493(2004)132<1721:SACAOO>2.0.CO;2.

Stoelinga, M. T., and Coauthors, 2003: Improvement of Microphysical Parameterization through Observational Verification Experiment. *Bull. Amer. Meteor. Soc.*, **84**, 1807–1826, https://doi.org/10.1175/BAMS-84-12-1807.

Testud, J., S. Oury, R. A. Black, P. Amayenc, and X. Dou, 2001: The concept of "normalized" distribution to describe raindrop spectra: A tool for cloud physics and cloud remote sensing. *J. Appl. Meteor.*, **40**, 1118–1140, https://doi.org/10.1175/1520-0450(2001)040<1118:TCONDT>2.0.CO;2.

Thompson, E. J., S. A. Rutledge, B. Dolan, and M. Thurai, 2015: Drop size distributions and radar observations of convective and stratiform rain over the equatorial Indian and west Pacific Oceans. *J. Atmos. Sci.*, **72**, 4091–4125, https://doi.org/10.1175/JAS-D-14-0206.1.

Tokay, A., D. B. Wolff, and W. A. Petersen, 2014: Evaluation of the new version of the laser-optical disdrometer, OTT Parsivel^2. *J. Atmos. Oceanic Technol.*, **31**, 1276–1288, https://doi.org/10.1175/JTECH-D-13-00174.1.

Ulbrich, C. W., 1983: Natural variations in the analytical form of the raindrop size distribution. *J. Climate Appl. Meteor.*, **22**, 1764–1775, https://doi.org/10.1175/1520-0450(1983)022<1764:NVITAF>2.0.CO;2.

Viale, M., R. A. Houze Jr., and K. L. Rasmussen, 2013: Upstream orographic enhancement of a narrow cold-frontal rainband approaching the Andes. *Mon. Wea. Rev.*, **141**, 1708–1730, https://doi.org/10.1175/MWR-D-12-00138.1.

Warner, M. D., C. F. Mass, and E. P. Salathé, 2012: Wintertime extreme precipitation events along the Pacific Northwest coast: Climatology and synoptic evolution. *Mon. Wea. Rev.*, **140**, 2021–2043, https://doi.org/10.1175/MWR-D-11-00197.1.

White, A. B., P. J. Neiman, F. M. Ralph, D. E. Kingsmill, and P. O. G. Persson, 2003: Coastal orographic rainfall processes observed by radar during the California Land-falling Jets Experiment. *J. Hydrometeor.*, **4**, 264–282, https://doi.org/10.1175/1525-7541(2003)4<264:CORPOB>2.0.CO;2.

——, ——, J. M. Creamean, T. Coleman, F. M. Ralph, and K. A. Prather, 2015: The impacts of California's San Francisco Bay Area gap on precipitation observed in the Sierra Nevada during HMT and CalWater. *J. Hydrometeor.*, **16**, 1048–1069, https://doi.org/10.1175/JHM-D-14-0160.1.

Willis, P. T., 1984: Functional fits to some observed drop size distributions and parameterization of rain. *J. Atmos. Sci.*, **41**, 1648–1661, https://doi.org/10.1175/1520-0469(1984)041<1648:FFTSOD>2.0.CO;2.

Zhu, Y., and R. E. Newell, 1994: Atmospheric rivers and bombs. *Geophys. Res. Lett.*, **21**, 1999–2002, https://doi.org/10.1029/94GL01710.

——, and ——, 1998: A proposed algorithm for moisture fluxes from atmospheric rivers. *Mon. Wea. Rev.*, **126**, 725–735, https://doi.org/10.1175/1520-0493(1998)126<0725:APAFMF>2.0.CO;2.